

RESEARCH ARTICLE

10.1029/2021JD035284

Key Points:

- WRF 4-km early-spring SWE underestimates are due to strong melting caused by enhanced sensible heat to snow and solar radiation absorption
- The enhanced surface heat exchange coefficient and thus sensible heat flux to snowpack are driven by strong surface winds in the WRF model
- The enhanced solar radiation absorption is due to strong surface downward solar radiation and strong melting-induced snow cover reduction

Supporting Information:

Supporting Information may be found in the online version of this article.

Correspondence to:

C. He,
cenlinhe@ucar.edu





Citation:

He, C., Chen, F., Abolafia-Rosenzweig, R., Ikeda, K., Liu, C., & Rasmussen, R. (2021). What causes the unobserved early-spring snowpack ablation in convection-permitting WRF modeling over Utah mountains? *Journal of Geophysical Research: Atmospheres*, 126, e2021JD035284. <https://doi.org/10.1029/2021JD035284>

Received 18 MAY 2021

Accepted 3 NOV 2021

What Causes the Unobserved Early-Spring Snowpack Ablation in Convection-Permitting WRF Modeling Over Utah Mountains?

Cenlin He¹ , Fei Chen¹ , Ronnie Abolafia-Rosenzweig¹ , Kyoko Ikeda¹ ,
Changhai Liu¹, and Roy Rasmussen¹

¹Research Applications Laboratory, National Center for Atmospheric Research, Boulder, CO, USA

Abstract Accurate prediction of snowpack evolution and ablation is critical to supporting weather and hydrological applications. Convection-permitting modeling has been shown to well capture observed snowpack evolution over many western United States (U.S.) mountain ranges, but some significant ablation biases still remain. In this study, we conduct process-level snowpack analyses of a widely used convection-permitting (4-km) weather research and forecasting (WRF) modeling product (WRF4km) for the contiguous U.S. to understand the mechanisms causing its unobserved early-spring snow ablation over Utah mountains. Analyses across Utah Snowpack Telemetry (SNOTEL) sites show that the unobserved snowpack ablation during mid-February to late-March in WRF4km is driven by multiple strong melting events. The melting results from the enhanced downward sensible heat flux to snowpack and enhanced ground solar radiation absorption, with generally larger contributions from the former before early March and from the latter after early March. The enhanced downward sensible heat flux to snowpack is mainly due to the enhanced surface heat exchange coefficient induced by high surface wind speeds. The enhanced ground solar radiation absorption is driven by both enhanced surface downward solar radiation and strong melting-induced snow cover reduction that is caused by deficiencies in Noah-MP snow-related parameterizations used in WRF4km. The substantial snow cover reduction during melting decreases surface albedo and hence triggers a positive albedo feedback that further accelerates melting. Our analyses reveal possible deficiencies in WRF and Noah-MP (e.g., canopy processes and snow albedo) and shed light on future directions for model improvements.

Plain Language Summary Snowpack plays an important role in modulating surface energy and water balance and land-atmosphere interaction in the Earth system. Snow melting is key to many important hydrological applications by affecting runoff, fresh water availability, and drought, particularly over western United States (U.S.) mountainous regions. Convection-permitting modeling with a high spatial resolution (e.g., ≤ 4 km) can accurately capture observed snowpack evolution over many western U.S. mountain ranges, but some important melting biases still remain. In this study, we conduct analyses of the widely used 4-km weather research and forecasting (WRF) modeling product developed at the National Center for Atmospheric Research to understand the reasons causing its strong early-spring snow melting over Utah mountains, which is not seen in observations. We find that the strong melting during mid-February to late-March in the model is due to (a) the enhanced downward sensible heat flux to snowpack driven by strong surface winds, and (b) the enhanced ground absorption of solar radiation caused by strong surface downward solar radiation and strong snow cover reduction induced by melting. Our results reveal possible deficiencies in model physics (e.g., canopy processes and snow albedo) and shed light on future directions for model improvements.

1. Introduction

Snowpack plays a key role in modulating surface energy and water balance and land-atmosphere interaction in the Earth system (e.g., Chen et al., 2014; Xu & Dirmeyer, 2011). The ablation of snowpack, in particular, is critical to many important hydrological applications by affecting snowmelt-driven runoff, fresh water availability, and drought (e.g., Barnett et al., 2005; Bales et al., 2006; Barnhart et al., 2016; Xiao et al., 2021). In the western United States (U.S.), snowmelt contributes to more than 50% of total runoff (Li et al., 2017), which provides freshwater supply to large populations. Over the past decades, the western U.S.

snowpack has been significantly declining under the warming climate (e.g., Mote et al., 2018; Pederson et al., 2011), and the declining trend is very likely to continue in the future (e.g., Gergel et al., 2017; Rhoades et al., 2018; Sun et al., 2019). The declining snowpack is often associated with earlier snowmelt and shorter snow seasons, causing earlier runoff, reduced streamflow magnitude in late spring and summer, and hence increased drought risks (e.g., Livneh & Badger, 2020; Luce & Holden, 2009; Musselman et al., 2017; Stewart et al., 2005). Thus, accurate prediction of the evolution and ablation of the western U.S. snowpack is critically important for supporting hydrological applications and water resource management.

Several factors can affect snowpack ablation (melting and sublimation), including meteorological forcing (e.g., surface temperature, wind, and radiation), snowpack physics, and land surface properties. For example, surface temperature is one of the dominant factors controlling snow melting (Bales et al., 2006; Mote et al., 2018). Wind drives both snow drifting and sublimation (Clark et al., 2011; Molotch et al., 2007). Solar radiation often provides the energy for snowpack heating and hence ablation (Burles & Boon, 2011; Harpold et al., 2014; Painter et al., 2018). Vegetation impacts snow ablation through complex snow-canopy interactions such as canopy interception, blocking of solar radiation, canopy longwave radiation, wind attenuation, and below-canopy turbulence (Essery et al., 2009; Mazzotti et al., 2019; Webster et al., 2016; Xiao et al., 2021). Topography (elevation, slope, and aspect) affects surface temperature and radiation and subsequently snow ablation in mountain environments (Clark et al., 2011; Liston, 2004). In addition, deposition of light-absorbing particles reduces snow albedo, which enhances snowpack absorption of solar radiation and thus melting (He, Liou, et al., 2019; He et al., 2018; Painter et al., 2012).

In the past decade, substantial efforts have been made to improve snowpack simulations over complex terrain in the western U.S., including the use of high-resolution (e.g., convection-permitting) modeling (e.g., Chen et al., 2019; Ikeda et al., 2010; Liu et al., 2011, 2017; Prein et al., 2015; Rasmussen et al., 2011, 2014). In particular, with proper model configurations, convection-permitting (typically ≤ 4 km) simulations can accurately capture the observed precipitation and snowpack evolution over many western U.S. mountainous regions (He, Chen, et al., 2019; Jing et al., 2017; Lundquist et al., 2019; Wang et al., 2018). One widely used convection-permitting modeling product covering the contiguous U.S. (CONUS) is the 4-km weather research and forecasting (WRF) simulation (Liu et al., 2017) developed at the National Center for Atmospheric Research (NCAR). This product has been comprehensively evaluated and applied to various snow-related analyses (e.g., Eidhammer et al., 2018; He, Chen, et al., 2019; Ikeda et al., 2021; Musselman et al., 2017, 2018, 2021).

However, recent studies analyzing the 4-km NCAR WRF CONUS simulation against the Snowpack Telemetry (SNOTEL) measurements revealed that although the simulation captures total precipitation reasonably well, it shows strong snow ablation in early spring at many SNOTEL sites, particularly over Utah mountains, which is not seen in observations (He, Chen, et al., 2019; Ikeda et al., 2021). This leads to a significant model underestimate in the timing and magnitude of peak snow water equivalent (SWE) in those areas. Nevertheless, the underlying mechanisms causing this model ablation bias have not been investigated in detail. A better understanding of factors and processes driving the unobserved early-spring snow ablation in the model can provide physical insights for future land and weather model improvements, and have important implications for enhanced predictions and projections of snowpack, weather, and hydrology.

Therefore, this study investigates the strong early-spring snow ablation in the convection-permitting NCAR WRF CONUS simulation via process-level analyses at SNOTEL sites. Our objective is to answer three scientific questions: (a) what drives the early-spring snow ablation in the WRF model? (b) what are the relative roles of atmospheric forcing and model snow physics? (c) how could the snowpack simulation be improved? This study focuses on the Utah mountains, where the aforementioned model ablation bias is the most prominent (He, Chen, et al., 2019; Ikeda et al., 2021). The analysis in this study could also shed light on diagnosing model ablation biases in other mountainous regions.

In this paper, we describe observational and modeling datasets as well as the method of surface water and energy budget analysis in Section 2. We present results and discussions of the mechanisms driving the model snow ablation bias in Section 3. We discuss uncertainties and implications for future model improvements in Section 4. Finally, we conclude the study in Section 5.

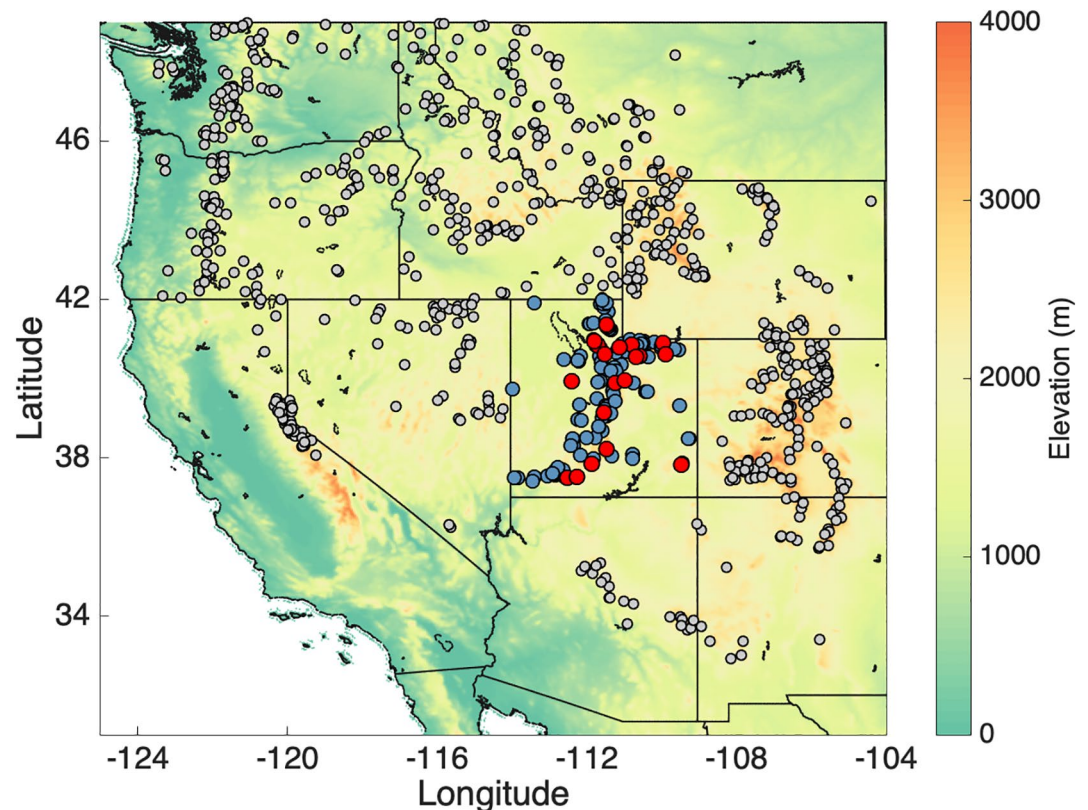


Figure 1. The topography (background map) and locations of SNOTEL sites over the Utah mountains (blue dots) and the other western U.S. mountains (gray dots). The Utah sites used for in-depth analysis are marked by red dots.

2. Methods and Data Sets

2.1. SNOTEL Observation

We use the daily SNOTEL measurements of SWE, snow depth, precipitation, and surface temperature at 804 western U.S. mountain sites (Figure 1), which are operated by the Natural Resources Conservation Service (NRCS; Serreze et al., 1999). To minimize the data uncertainty, we adopt the bias-corrected and quality-controlled (BCQC) SNOTEL data (available at <https://www.pnnl.gov/data-products>) developed at the U.S. Pacific Northwest National Laboratory (PNNL). The BCQC procedures include removing outliers and erroneous measured values (e.g., negative SWE), adjusting erroneous precipitation and temperature values, eliminating inconsistent SWE and precipitation values (e.g., SWE exceeds precipitation by 5%), and correcting temperature and precipitation (e.g., snowfall under-catch) biases. More details of the BCQC algorithm can be found in Yan et al. (2018) and Sun et al. (2019). Our snow analysis for observations and model simulations in this study focuses on the SNOTEL sites over Utah mountains, except for optimizing the reference model configuration based on all SNOTEL sites (see Section 2.4.1). We select Utah sites with continuous BCQC data during the 2009–2013 water years, which reduces the number of Utah sites from 131 to 55 in our analysis.

2.2. WRF 4-km Simulation

We analyze the NCAR convection-permitting (4-km) WRF CONUS modeling product (hereinafter WRF4km; Liu et al., 2017, <https://rda.ucar.edu/datasets/ds612.0/>) to understand its unrealistically fast early-spring snow ablation over Utah SNOTEL sites (Ikeda et al., 2021; see also Figure 4a and Figures S5a–S9a in Supporting Information S1). The WRF4km simulation is based on the WRF version 3.4.1 driven by boundary conditions from the ERA-Interim reanalysis meteorology (Dee et al., 2011) with spectral nudging. Main physics schemes used in WRF4km include the Rapid Radiative Transfer Model for General Circulation

Models (RRTMG) shortwave and longwave radiation scheme (Iacono et al., 2008), the Yonsei University (YSU) planetary boundary layer scheme (Hong et al., 2006), the revised Monin–Obukhov surface layer scheme (Jimenez et al., 2012), the Thompson cloud microphysics scheme (Thompson & Eidhammer, 2014), and the Noah with Multi-Parameterization (Noah-MP) land surface model (LSM; Niu et al., 2011), while the cumulus parameterization is de-activated (i.e., convection-permitting). In particular, the rainfall-snowfall partitioning is controlled by the cloud microphysics scheme (Thompson and Eidhammer, 2014). The snow albedo is determined by the Canadian Land Surface Scheme (CLASS) scheme (Verseghy, 1991) embedded in the Noah-MP LSM. More details of the WRF4km simulation can be found in Liu et al. (2017).

2.3. Noah-MP Model Description

Noah-MP is a state-of-the-art LSM enhanced from the community Noah LSM (Chen & Dudhia, 2001; Chen et al., 1996, 1997; Ek et al., 2003) through including physical representations of a separate vegetation canopy layer and multi-layer snowpack processes as well as multiple physics options for key land surface processes (Niu et al., 2011). Noah-MP has been implemented as a land component of the community WRF model and the U.S. operational National Water Model. Details of Noah-MP and its snowpack treatment have been documented in Niu et al. (2011) and Chen et al. (2014). Here we summarize the key model features related to snow processes. Noah-MP partitions rainfall and snowfall based on surface temperature with multiple parameterization options. The canopy-snow interception and throughfall processes are accounted for, including the evolution of both canopy snow (snowfall loading and unloading, frost, sublimation, and melting) and canopy liquid water (rainfall loading and unloading, dew, evaporation, and refreezing; Niu & Yang, 2004). The canopy-radiation interaction is treated by the two-stream radiative transfer approximation (Niu et al., 2011). Noah-MP simulates up to three ground snowpack layers by accounting for sublimation, frost, melting, interlayer movement of meltwater, and layer compaction. The snow albedo is computed by either the CLASS scheme (Verseghy, 1991) or the Biosphere-Atmosphere Transfer Scheme (BATS; Dickinson et al., 1993), both accounting for the albedo decay due to snow aging. The snow cover fraction on the ground is determined by snow density, snow depth, and tunable snow cover parameters (Niu & Yang, 2007).

2.4. Noah-MP Simulations and Experiment Design

To understand and isolate the causes for the early-spring snow ablation bias in WRF4km, we conduct a suite of point-scale Noah-MP offline simulations at SNOTEL sites to compare with WRF4km, including one reference simulation (see Section 2.4.1) and five sensitivity simulations (see Section 2.4.2). Table 1 summarizes the key differences in atmospheric forcing and model configurations among these simulations. For these Noah-MP offline simulations, we spin up the model for 10 years and output hourly results. We use the 30-m land cover data from the 2016 National Land Cover Database (NLCD; <https://www.mrlc.gov/data>), which is different from the one used in WRF4km that is based on the 1-km Moderate Resolution Imaging Spectroradiometer (MODIS) land cover data (http://www2.mmm.ucar.edu/wrf/users/download/get_sources_wps_geog.html). Based on our tests, using these two different land type data sets only has minor effects on the Noah-MP snow simulations and analyses, and does not contribute to the SWE differences between WRF4km and Noah-MP offline simulations (not shown), which thus does not change the conclusions of this study. Note that there may also be some inconsistency in vegetation type between the 30-m NLCD data set and the actual field at SNOTEL sites. However, given the good agreement between the observed and modeled SWE and snow depth across SNOTEL sites in this study (see below), the use of the high-resolution NLCD data set allows the model to accurately simulate the mean effect of vegetation on snowpack observed at SNOTEL locations.

2.4.1. Reference Simulation

To isolate the causes of the snow ablation bias in WRF4km, we compare WRF4km with a reference simulation that is able to accurately capture observed snowpack evolution at SNOTEL sites. We use optimized atmospheric forcing (hereinafter the reference forcing) and improved Noah-MP model configuration (hereinafter the reference configuration) in our reference simulation (hereinafter NoahMP-ref; see also Table 1). Specifically, to generate the reference forcing, we first downscale the atmospheric forcing (i.e., precipitation, surface temperature, humidity, wind, pressure, shortwave, and longwave downward radiation) from the

Table 1
Model Experiments Designed in This Study

| Simulations | Descriptions | Atmospheric forcing | Noah-MP configuration | Hypothesis for experiment design |
|------------------------------|---|--|---|--|
| WRF4km | Coupled WRF/Noah-MP 4-km simulation | 4-km WRF simulation | Configuration embedded in WRF4km ^a | – |
| NoahMP-ref | Offline Noah-MP simulation with reference configuration and reference forcing | Reference forcing ^b | Reference configuration ^c | Designed to compare with WRF4km to test the hypothesis that errors in snow physics and atmospheric forcing in WRF4km contribute to WRF4km snow ablation bias |
| NoahMP-WRFforc | Offline Noah-MP simulation with reference configuration and WRF4km forcing | WRF4km forcing | Reference configuration | Designed to compare with WRF4km and NoahMP-ref to test the hypothesis that errors in snow physics and atmospheric forcing, respectively, contribute to WRF4km snow ablation bias |
| NoahMP-WRFforc-refWind | Same as NoahMP-WRFforc except the use of reference wind forcing | WRF4km forcing with wind replaced by reference forcing | Reference configuration | Designed to compare with NoahMP-WRFforc to test the hypothesis that surface wind error in WRF4km contributes to WRF4km snow ablation bias |
| NoahMP-WRFforc-refWind-refSW | Same as NoahMP-WRFforc-refWind except the use of reference downward solar radiation forcing | WRF4km forcing with wind and downward solar radiation replaced by reference forcing | Reference configuration | Designed to compare with NoahMP-WRFforc-refWind to test the hypothesis that downward solar radiation error in WRF4km contributes to WRF4km snow ablation bias |
| NoahMP-ref-windtest | Same as NoahMP-ref except limiting wind speed to $\leq 2 \text{ m s}^{-1}$ | Reference forcing with wind speed limited to $\leq 2 \text{ m s}^{-1}$ | Reference configuration | Designed to compare with NoahMP-ref to test the hypothesis that surface wind error in NoahMP-ref contributes to NoahMP-ref snow ablation bias |
| NoahMP-ref-windtest-SWtest | Same as NoahMP-ref-windtest except reducing downward solar radiation by 20% | Reference forcing with wind speed limited to $\leq 2 \text{ m s}^{-1}$ and downward solar radiation reduced by 20% | Reference configuration | Designed to compare with NoahMP-ref-windtest to test the hypothesis that downward solar radiation error in NoahMP-ref contributes to the NoahMP-ref snow ablation bias |

^aNoah-MP configuration embedded in WRF4km: Old Noah-MP version released in WRFv3.4; cloud microphysics-based rain-snow partitioning; CLASS snow albedo scheme; other Noah-MP snow-relevant physics options are the same as the reference configuration (see below). ^bReference forcing: forcing downscaled from hourly 0.125° NLDAS-2 data to 90-m spatial resolution with topographic adjustment following Liston and Elder (2006) and Gupta and Tarboton (2016); precipitation and surface temperature further scaled to match daily SNOTEL observations. ^cReference Noah-MP configuration: latest Noah-MP version released in WRFv4.3 with updated snow cover parameters; best-performed Noah-MP physics option setup (Table S1 in Supporting Information S1) based on sensitivity tests (Figure S1 in Supporting Information S1); additional model enhancements by improving surface roughness length formulation and snow compaction rate (Figure S2 and Text S1–S2 in Supporting Information S1).

hourly 0.125° North American Land Data Assimilation System version 2 data (NLDAS-2; Xia et al., 2012) to 90-m spatial resolution with topographic adjustments following Liston and Elder (2006) and Gupta and Tarboton (2016). Then, we further scale the hourly precipitation forcing by the ratio of daily total precipitation from SNOTEL observations to that from the downscaled NLDAS-2 forcing so that the daily total precipitation forcing is the same as observations. Similar scaling is also done for hourly temperature forcing so that the daily mean temperature forcing is the same as SNOTEL observations.

To generate the reference model configuration, we make four progressive Noah-MP updates in a step-by-step manner (as shown below) by evaluation against SNOTEL measurements in the western U.S. We use all the western U.S. SNOTEL sites (instead of Utah sites only) to assess the reference simulation, because we seek to improve the snow-related model processes to allow stronger robustness and broader applicability of the community Noah-MP model schemes across different mountain ranges with different snow and climate conditions. Qualitative results and conclusions presented in this study are insensitive to the optimization of the reference simulation across the broader western U.S. rather than only Utah sites; however, minor quantitative uncertainties are introduced (see Section 4 for more discussions).

1. We first use the latest Noah-MP version (<https://github.com/NCAR/hrlDas>) released along with WRF version 4.3, where the tunable snow cover parameters are specified as a function of land-cover types to mitigate cold temperature bias over snow-covered areas in the WRF simulations (e.g., WRF4km; He, Chen, et al., 2019).
2. We then conduct a series of sensitivity simulations by varying Noah-MP physics options for key snow-related processes, and select the best-performed physics option configuration that agrees best with SNOTEL SWE measurements (Figure S1 and Table S1 in Supporting Information S1). Note that the BATS snow albedo scheme is used in our best-performed physics option configuration, which is different from the one (the CLASS scheme) used in WRF4km. However, changing the BATS to CLASS snow albedo scheme does not change SWE simulations at SNOTEL sites in our sensitivity tests (Figure S1 in Supporting Information S1).
3. The default surface-layer parametrization in Noah-MP (i.e., the SFCDF1 scheme) assumes the same surface roughness length for scalar (i.e., heat and moisture) and momentum fluxes (such as used in WRF4km), whereas previous studies pointed out that these roughness lengths are different due to different mechanisms and resistances controlling momentum and heat transfer (Chen & Zhang, 2009; Chen et al., 1997; Zilitinkevich, 1995). Thus, we enhance the SFCDF1 scheme in this study by adding the formulation of Zilitinkevich (1995) and Chen and Zhang (2009) for the roughness length of heat and moisture fluxes (see Text S1 in Supporting Information S1), which further reduces model SWE underestimates over short-vegetated sites (Figure S2 in Supporting Information S1). This is because updating the roughness length formulation reduces the below-canopy exchange coefficient for heat and moisture and hence decreases upward latent heat flux and downward sensible heat flux at snowpack surface in the model (Figure S3 in Supporting Information S1), resulting in reduced snow sublimation and melting.
4. Finally, with all the preceding updates, Noah-MP still underestimates snow depth, although SWE is accurately captured (Figure S2 in Supporting Information S1). This suggests that snowpack compaction process may be biased in the model. Noah-MP accounts for three snowpack compaction processes driven by destructive metamorphism, overburden, and melting, respectively, following the Anderson (1976) parameterizations. Our sensitivity analyses indicate that snow depth simulations at SNOTEL sites are most sensitive to the overburden-induced compaction, which is a function of snow mass load and viscosity coefficient (see Text S2 in Supporting Information S1). We also note that the snow viscosity coefficient at 0°C, a key parameter controlling the overburden-induced compaction rate, is associated with large uncertainty (Anderson, 1976), and its default value ($0.8 \times 10^6 \text{ kg s m}^{-2}$) used in Noah-MP is toward the lower bound of the suggested range (0.52×10^6 – $7.62 \times 10^6 \text{ kg s m}^{-2}$) for LSMs (Anderson, 1976; van Kampenhout et al., 2017; Sun et al., 1999). Thus, we increase the viscosity coefficient to $1.33 \times 10^6 \text{ kg s m}^{-2}$ to best match the SNOTEL observations of snow depth (Figure S2 in Supporting Information S1), which thus reduces the overburden-induced snow compaction rate and model underestimates of snow depth. We note that this update of snow compaction rate also increases snow cover fraction in Noah-MP as a result of larger snow depth.

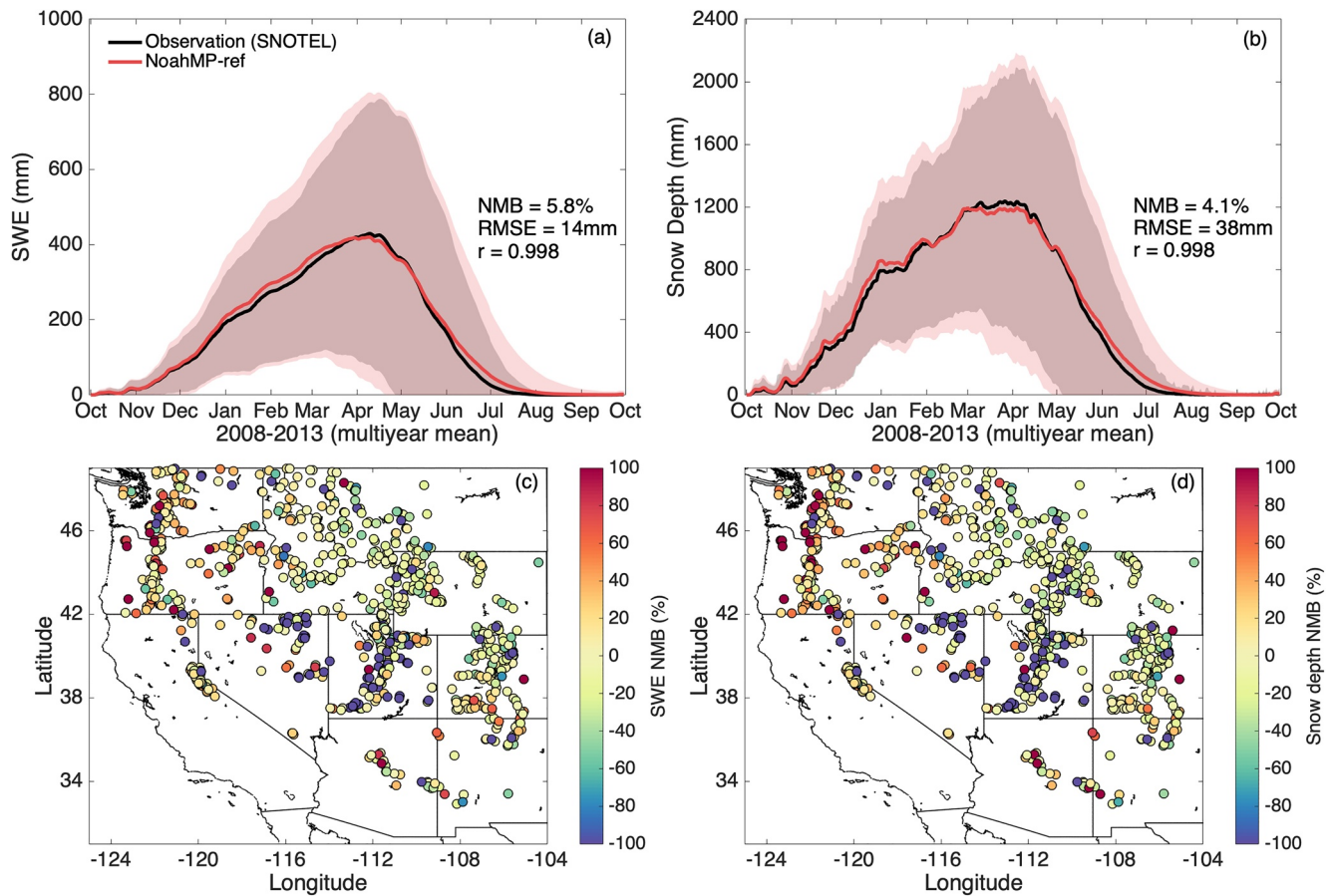


Figure 2. (a) Daily snow water equivalent (SWE) from SNOTEL observations (black) and the Noah-MP reference simulation (NoahMP-ref; red) averaged across SNOTEL sites in the western U.S. during 2009–2013 water years. Red and black shaded areas are one-standard-deviations of the site-wise variability. Also shown are the normalized mean bias (NMB; mean model bias normalized by observational mean), root-mean-square-error (RMSE), and correlation (r). (b) Same as (a), but for daily snow depth. (c) Annual mean NMB of SWE at each SNOTEL site for the Noah-MP reference simulation averaged during 2009–2013 water years. (d) Same as (c), but for snow depth.

Based on the reference model configuration driven by the reference forcing, NoahMP-ref well reproduces the observed SWE and snow depth averaged across SNOTEL sites in the western U.S. (Figures 2a and 2b), with annual mean normalized biases (NMB) of 5.8% and 4.1%, root-mean-square-errors (RMSE) of 14 and 38 mm, and correlation coefficients (r) of 0.998 and 0.998 for SWE and snow depth, respectively. The spatial distribution of the model bias also shows high heterogeneity, with <20% NMB over a large portion of sites but sizable underestimates of SWE and snow depth at some Utah sites (Figures 2c and 2d) partially due to the ablation bias as discussed in Sections 3.5 and 4. Further analyses reveal a negative correlation between annual wind speeds and SWE NMB across SNOTEL sites (Figure S4 in Supporting Information S1), with SWE biases changing from positive to negative values as wind speeds increase. In this study, we compare NoahMP-ref with WRF4km to quantify the effects of atmospheric forcing and land model physics on snow-pack simulations in Section 3.

2.4.2. Sensitivity Simulations

To further quantify the role of atmospheric forcing in contributing to the WRF4km snow ablation bias, we conduct several additional Noah-MP offline sensitivity simulations using the reference model configuration (Section 2.4.1) but driven by different forcing conditions (Table 1). The first sensitivity simulation is the same as NoahMP-ref except using the WRF4km forcing (hereinafter NoahMP-WRFforc). The comparison between NoahMP-ref and NoahMP-WRFforc reveals the effect of the WRF4km forcing, while the comparison between NoahMP-WRFforc and WRF4km reflects the effect of snow-related parameterizations in Noah-MP. The second sensitivity simulation (hereinafter NoahMP-WRFforc-refWind) is the same

as NoahMP-WRFforc except replacing the WRF4km wind forcing with the reference wind forcing (i.e., wind speed from the reference forcing described in Section 2.4.1). The comparison between NoahMP-WRFforc-refWind and NoahMP-WRFforc is used to quantify the effect of wind forcing. The third sensitivity simulation (hereinafter NoahMP-WRFforc-refWind-refSW) is the same as NoahMP-WRFforc-refWind except further replacing the WRF4km downward solar radiation forcing with the reference solar radiation forcing (i.e., solar radiation from the reference forcing described in Section 2.4.1). The comparison between NoahMP-WRFforc-refWind-refSW and NoahMP-WRFforc-refWind is used to quantify the effect of solar radiation forcing. The fourth sensitivity simulation (hereinafter NoahMP-ref-windtest) is the same as NoahMP-ref except limiting wind forcing to $\leq 2 \text{ m s}^{-1}$ based on preliminary analyses. The comparison between NoahMP-ref-windtest and NoahMP-ref is used to investigate the effect of wind forcing on snow bias in the reference simulation. The fifth sensitivity simulation (hereinafter NoahMP-ref-windtest-SWtest) is the same as NoahMP-ref-windtest except further reducing downward solar radiation forcing by 20% based on preliminary analyses. The comparison between NoahMP-ref-windtest-SWtest and NoahMP-ref-windtest is used to investigate the effect of solar radiation forcing on snow bias in the reference simulation. Overall, the intercomparison among the preceding sensitivity simulations and NoahMP-ref reveals the effect of the tested forcing variables on snow simulations (see Section 3).

2.5. Energy and Water Budget Analysis at Snowpack Surface

To understand the mechanisms driving the WRF4km snow ablation bias, we conduct process-level analyses of snow surface energy and water budget at selected Utah SNOTEL sites (Figure 1) based on the aforementioned model simulations (Sections 2.2 and 2.4). We analyze eight representative sites (Table S2 in Supporting Information S1) where NoahMP-ref accurately captures observed SWE but WRF4km shows the early-spring snow ablation bias. We divide these sites into three types with the ablation bias dominated by deficiencies in either atmospheric forcing, or snow-related model parameterization, or both. The criterion to categorize the sites dominated by deficiencies in forcing is that NoahMP-ref accurately captures the observed early-spring SWE, but WRF4km and NoahMP-WRFforc both show a similar early-spring ablation bias. The criterion to categorize the sites dominated by deficiencies in model snow parameterizations is that both NoahMP-ref and NoahMP-WRFforc accurately capture the observed early-spring SWE, but WRF4km shows a strong early-spring ablation bias. The criterion to categorize the sites dominated by deficiencies in both forcing and snow parameterizations is that NoahMP-ref accurately capture the observed early-spring SWE, and WRF4km shows a strong early-spring ablation bias, with NoahMP-WRFforc performing better than WRF4km but worse than NoahMP-ref. To further understand the possible deficiency in the NoahMP-ref configuration and physics, we analyze eight additional sites (Table S2 in Supporting Information S1) where NoahMP-ref also shows the early-spring ablation bias. In this study, we focus on the period of mid-February to late March (i.e., early spring).

For the snow surface energy balance, Noah-MP accounts for eight major energy fluxes (Figure 3a), including downward and upward shortwave (SW) and longwave (LW) radiation, sensible heat (SH), latent heat (LH), ground heat (G) flux into snowpack and soil that directly drives snow and soil temperature change and melting/refreezing, and heat advected to the surface by precipitation (PH) due to temperature differences between the surface and the air, based on the following energy balance equation:

$$\text{netRad} + \text{PH} = \text{SH} + \text{LH} + \text{G} \quad (1)$$

$$\text{netRad} = \text{SW}_{\text{down}} - \text{SW}_{\text{up}} + \text{LW}_{\text{down}} - \text{LW}_{\text{up}} \quad (2)$$

where netRad is the net surface radiation. More details about SH calculations in Noah-MP are provided Text S1. Noah-MP simulates these fluxes over both bare and vegetated portions of each model grid based on the vegetation fraction (FVEG). For each flux term, the resulting grid-mean value (F_{grid}) at the snowpack-air interface is an average of the values over bare and vegetated (i.e., below-canopy) grounds weighted by FVEG as follows:

$$F_{\text{grid}} = F_v \times \text{FVEG} + F_b \times (1 - \text{FVEG}) \quad (3)$$

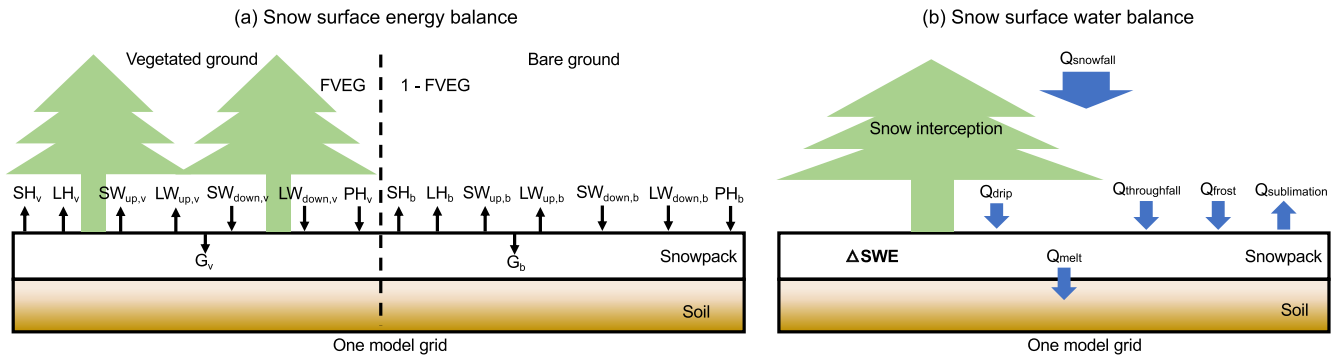


Figure 3. Demonstration of snow surface energy (a) and water (b) balance treatments in Noah-MP. (a) Energy fluxes over bare (“b” in the subscript) and vegetated (“v” in the subscript) parts of a model grid with a vegetation fraction (FVEG), including shortwave (SW) and longwave (LW) radiation, latent heat (LH), sensible heat (SH), heat into snowpack and soil (G) to drive melting, and heat advected to the surface by precipitation (PH) due to temperature differences between the surface and the air. (b) Snow water fluxes (Q) for total snowfall, drip from canopy-intercepted snow, snow throughfall, frost, sublimation, and melting, which together lead to net SWE change.

where F represents one of the aforementioned fluxes (i.e., SW, LW, PH, SH, LG, or G), and the subscripts b and v indicate fluxes over bare and vegetated grounds, respectively. As a result, the snowpack evolution in Noah-MP is driven by the grid-mean surface fluxes (F_{grid}), which are the results presented in the energy budget analysis (Sections 3.2–3.5). We do not include the PH term in our analysis, due to its rather small contribution to total surface energy budget (Chen et al., 2014). In Noah-MP, positive netRad indicates net downward radiative flux from the air to the ground, while positive SH and LH indicate upward heat fluxes from the ground to the air. Positive G indicates downward heat flux from the snowpack surface into underlying snow and soil layers.

For the snow surface water balance, Noah-MP account for five major water fluxes (Figure 3b), including drip of canopy-intercepted snowfall (Q_{drip}), throughfall of snowfall ($Q_{through}$), frost (Q_{frost}), sublimation (Q_{sub}), and melting (Q_{melt}), which together lead to net SWE change (ΔSWE), based on the following water balance equation:

$$\Delta SWE = Q_{drip} + Q_{through} + Q_{frost} - Q_{sub} - Q_{melt} \quad (4)$$

We note that the ground snowfall presented in the water budget analysis (Sections 3.2–3.5) is the sum of Q_{drip} and $Q_{through}$, while the total snowfall forcing presented in the forcing analysis (Section 3.1) is the above-canopy snowfall determined by total precipitation and rainfall-snowfall partitioning ratios. The difference between the above-canopy snowfall and the sum of Q_{drip} and $Q_{through}$ is the canopy-intercepted snow that does not reach the ground snowpack, including the intercepted snow staying at the canopy surface and related loss through sublimation of snow ice and evaporation of melted snow at the canopy surface.

3. Results and Discussions

3.1. Overall Site-Averaged Analysis

Figure 4 shows the observed and simulated daily atmospheric forcing and SWE evolution averaged across Utah SNOTEL sites. During the snow accumulation from November to early March, WRF4km underestimates SWE by up to ~100 mm (Figure 4a), which generally follows the trend of snowfall underestimates (Figure 4b), whereas NoahMP-ref accurately reproduces the observed SWE accumulation mainly due to the use of observed precipitation and temperature as forcing. The WRF4km snowfall underestimate is dominated by the total precipitation underestimate (Figures 4a and 4b), while the ratio of snowfall over total precipitation is almost the same for NoahMP-ref and WRF4km (Figure 4b). This suggests consistent rainfall-snowfall partitioning determined by the WRF4km cloud microphysics (Thompson & Eidhammer, 2014) and the temperature-based scheme (Jordan, 1991) in NoahMP-ref. WRF4km tends to have small ($\leq 1^\circ\text{C}$) cold biases in surface air temperature during the accumulation period (Figure 4c), which does not contribute to the SWE accumulation bias. The systematically higher surface downward solar radiation (by $\sim 20 \text{ W m}^{-2}$;

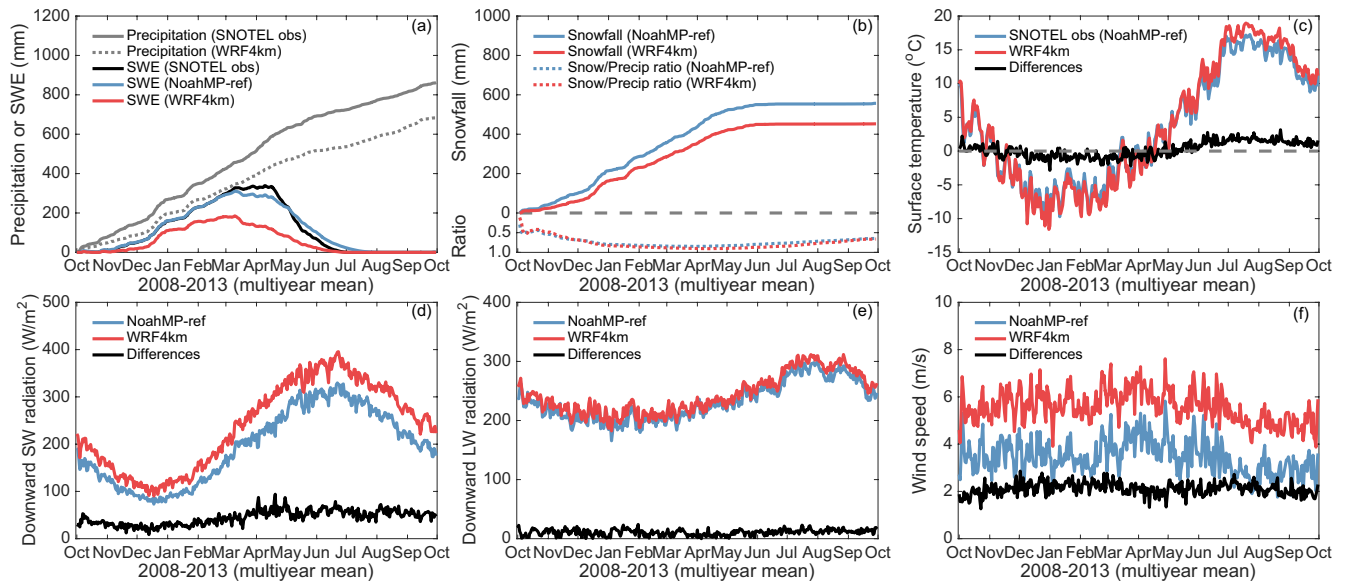


Figure 4. Daily mean atmospheric forcing and SWE averaged across 55 Utah SNOTEL sites during 2009–2013 water years. (a) Total precipitation from SNOTEL observations (gray solid line) and 4-km WRF simulations (gray dashed line; WRF4km), as well as SWE from SNOTEL observations (black), NoahMP reference simulations (blue; NoahMP-ref), and WRF4km (red). (b) Snowfall (solid lines) and the ratio of snowfall over total precipitation (dashed lines) from NoahMP-ref (blue) and WRF4km (red). (c) Surface temperature from SNOTEL observations (blue; used to drive NoahMP-ref as forcing) and WRF4km (red) as well as their differences (WRF4km minus observation). (d) Downward shortwave (SW) radiation from NoahMP-ref (blue) and WRF4km (red) as well as their differences (WRF4km minus NoahMP-ref). (e) Same as panel (d), but for downward longwave (LW) radiation. (f) Same as panel (d), but for wind speed.

Figure 4d) and wind speed (by $\sim 2 \text{ m s}^{-1}$; Figure 4f) during the accumulation period in WRF4km compared to NoahMP-ref may contribute to the WRF4km SWE underestimate through enhanced snowpack heating and sublimation. However, due to the very low surface temperature (below freezing point) during November to early March (Figure 4c), the contribution of higher downward solar radiation and wind speed to the SWE bias is small in this period.

In early March, the WRF4km SWE suddenly starts to decrease and continues decreasing throughout the rest of spring, whereas the observed SWE keeps a slight increase until mid-April (Figure 4a). This unobserved early-spring snow ablation bias in WRF4km is also consistent across each individual year (Figures S4–S8 in Supporting Information S1), which is not caused by the precipitation bias, since the observed precipitation trend in March is well captured by WRF4km (Figure 4a). On the other hand, the consistently stronger surface downward solar radiation (by up to 50 W m^{-2} ; Figure 4d) and wind speed (by $\sim 2 \text{ m s}^{-1}$; Figure 4f) during March can contribute to the ablation bias in WRF4km, as the surface temperature has increased to $\sim 0^\circ\text{C}$ (around the freezing point) in this period. Note that the preceding results are averages over all Utah SNOTEL sites, which may smooth out ablation bias signals and details at individual sites. Thus, to gain a more mechanistic understanding of the specific mechanisms causing the WRF4km ablation bias, we conduct detailed energy and water budget analyses at several typical sites in Sections 3.2–3.4. We note that NoahMP-ref also shows a slight SWE drop starting in early March, suggesting that the ablation bias also exists at some sites for NoahMP-ref. Thus, we also conduct detailed analyses at selected sites in Section 3.5 to understand the deficiency in NoahMP-ref.

3.2. Sites With Ablation Bias Driven by Atmospheric Forcing

Figure 5 shows the early-spring snow surface energy and water budget analysis for a typical SNOTEL site (Donkey Reservoir), where NoahMP-ref accurately captures the observed SWE accumulation during November to April but WRF4km and NoahMP-WRFforc both show a strong ablation starting in late February and continuing throughout March (Figure 5a). The similar ablation behaviors in WRF4km and NoahMP-WRFforc and their large differences from NoahMP-ref indicate that the ablation bias in WRF4km at this site is mainly driven by differences in the atmospheric forcing used in NoahMP-ref and WRF4km,

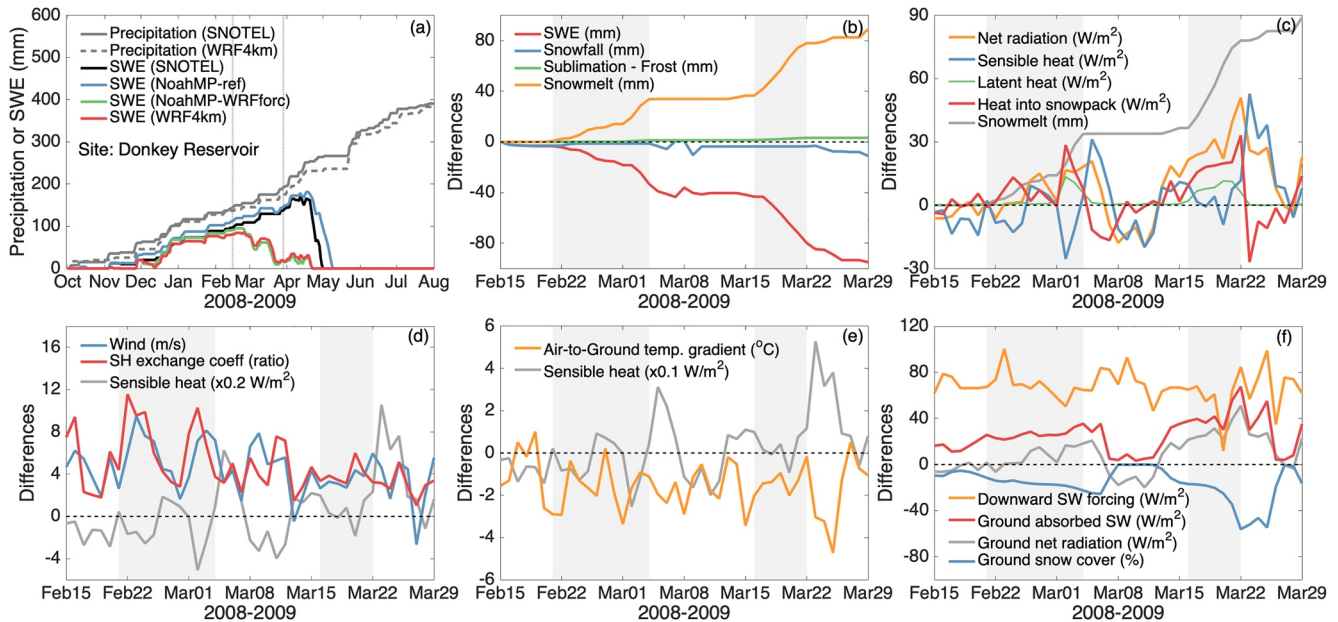


Figure 5. Energy and water budget analyses for the Donkey Reservoir SNOTEL site. (a) Daily precipitation from observations (gray solid line) and 4-km WRF simulations (gray dashed line; WRF4km), as well as SWE from observations (black), Noah-MP reference simulations (blue; NoahMP-ref), Noah-MP simulations driven by 4-km WRF forcing (green; NoahMP-WRFforc), and WRF4km (red). Analyses in panels (b)–(f) are conducted for the time period between two gray vertical dashed lines. (b) Differences between WRF4km and NoahMP-ref (the former minus the latter) in snow budget components (water accumulated since February 15), including SWE (red), snowfall (blue), net sublimation (green), and snowmelt (orange). Shaded time periods in (b)–(f) indicate melting events in WRF4km. (c) Same as panel (b), but for differences in daily mean net radiation (orange), sensible heat (blue), latent heat (green), and heat into snowpack (red) at snowpack surface. See text for definitions of the sign of each flux component. The melting curve (gray line) is shown as a reference. (d) Same as panel (b), but for differences in daily mean wind speed forcing (blue) and below-canopy sensible heat (SH) exchange coefficient (red); note that this difference is computed as a ratio of WRF4km divided by NoahMP-ref). The sensible heat curve (gray line) is shown as a reference. (e) Same as panel (b), but for differences in daily mean temperature gradient from air to ground (orange). (f) Same as panel (b), but for differences in daily mean downward shortwave (SW) radiation (orange), ground absorbed SW radiation (red), and ground snow cover (blue). The ground net radiation (gray line) is shown as a reference.

rather than differences in snow-related parameterizations and model configurations between them. Although WRF4km slightly underestimates the observed precipitation by <10% (Figure 5a), this precipitation underestimate does not contribute to the ablation from late February to late March in WRF4km. Further water budget analysis by comparing NoahMP-ref and WRF4km confirms that the early-spring SWE decrease is caused by several strong melting events in WRF4km rather than biases in snowfall or sublimation (Figure 5b). Each of these events has continuous snowmelt of 30–50 mm in less than 10 days.

Subsequent energy budget analyses reveal that, compared to NoahMP-ref, the strong melting events in WRF4km are primarily driven by the enhanced downward sensible heat flux (by up to 30 W m^{-2}) and the enhanced net radiation (by up to 60 W m^{-2}) at the snowpack surface, which both lead to a stronger heat flux into the snowpack directly driving the melting (Figure 5c). Particularly, the contribution of the enhanced downward sensible heat flux is more dominant in the melting event before early March, which is due to the 3–10 times higher surface (below-canopy) heat exchange coefficient induced by substantially stronger surface winds (by $2\text{--}9 \text{ m s}^{-1}$) in WRF4km (Figure 5d), instead of the increased air-to-ground temperature gradient (Figure 5e). On the other hand, the contribution of the enhanced net radiation increases since early March and becomes dominant in the late-March melting event (Figure 5c). This is because of the enhanced ground absorption of solar radiation, which is driven by both the systematically higher downward solar radiation forcing (by $40\text{--}80 \text{ W m}^{-2}$) and stronger melting-induced snow cover reductions (by up to 50%) in WRF4km, further reducing ground albedo and hence triggering a positive albedo feedback (Qu & Hall, 2006). In addition, energy and water budget analyses of NoahMP-WRFforc show very similar results and mechanisms driving the strong early-spring snow melting (Figure S10 in Supporting Information S1).

To further validate our explanation that the consistently higher wind speed and enhanced downward solar radiation forcing in WRF4km compared to NoahMP-ref are the drivers for the unobserved early-spring snow

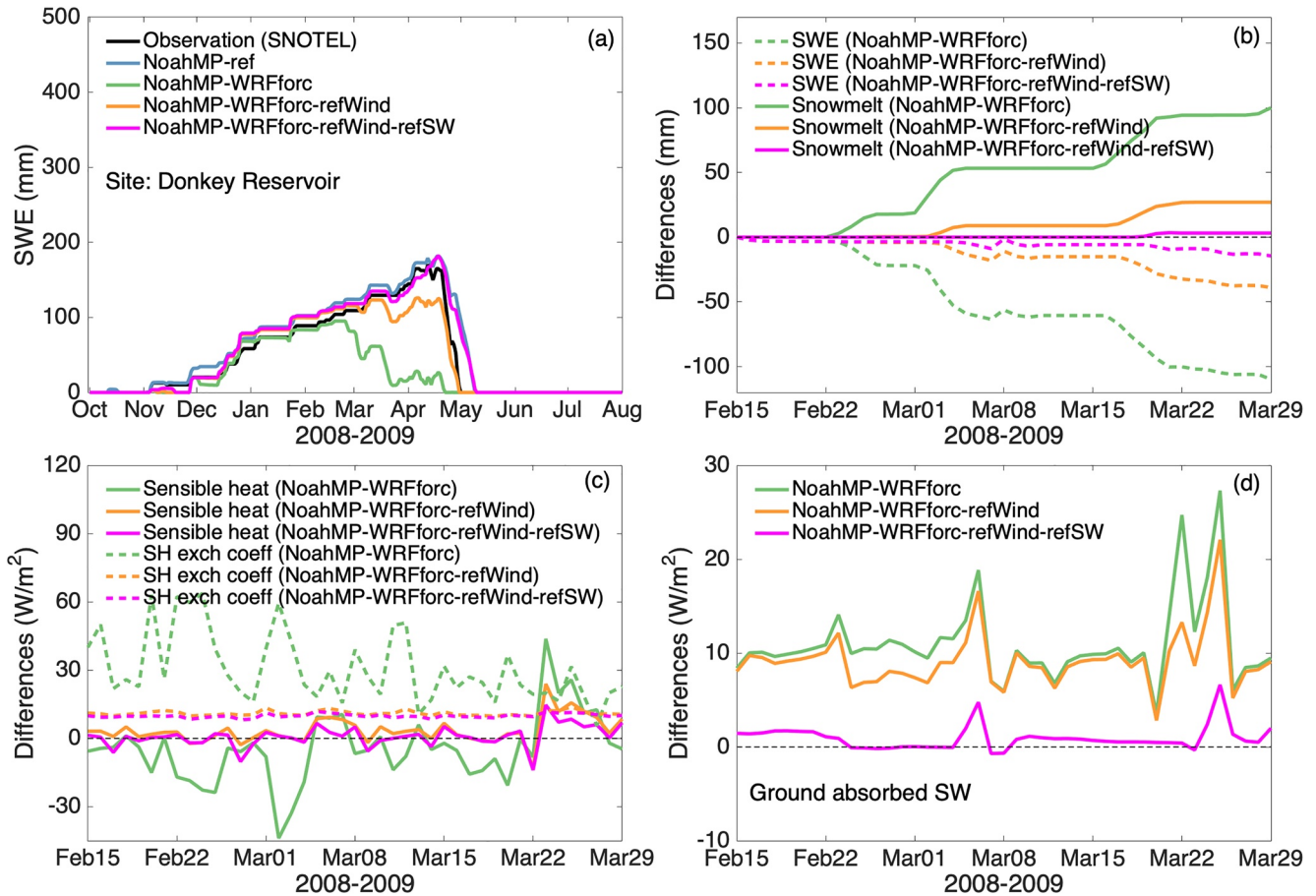


Figure 6. Sensitivity analyses at the Donkey Reservoir SNOTEL site for Noah-MP reference simulations (blue; NoahMP-ref), Noah-MP simulations driven by 4-km WRF forcing (green; NoahMP-WRFforc), Noah-MP simulations driven by wind speed from the reference forcing and other forcings from 4-km WRF simulations (orange; NoahMP-WRFforc-refWind), and Noah-MP simulations driven by wind speed and downward solar radiation from the reference forcing and other forcings from 4-km WRF simulations (magenta; NoahMP-WRFforc-refWind-refSW). (a) Daily SWE from observations (black), NoahMP-ref, NoahMP-WRFforc, NoahMP-WRFforc-refWind, and NoahMP-WRFforc-refWind-refSW simulations (b) Differences between sensitivity simulations (i.e., NoahMP-WRFforc, NoahMP-WRFforc-refWind, or NoahMP-WRFforc-refWind-refSW) and NoahMP-ref (the former minus the latter) for SWE (dashed lines) and snowmelt (solid lines) accumulated since February 15. (c) Same as panel (b), but for differences in daily mean below-canopy sensible heat flux (solid lines; $W m^{-2}$) and sensible heat (SH) exchange coefficient (multiplied by 10; dashed lines; expressed as ratios of sensitivity simulations divided by NoahMP-ref). (d) Same as panel (b), but for differences in daily mean ground absorbed shortwave (SW) radiation ($W m^{-2}$).

melting at this site, we compare NoahMP-WRFforc with NoahMP-WRFforc-refWind and NoahMP-WRFforc-refWind-refSW. The results indicate that replacing the WRF4km wind forcing with the NoahMP-ref wind forcing substantially reduces the below-canopy heat exchange coefficient and hence downward sensible heat flux to snowpack surface (Figure 6c), while replacing the WRF4km downward solar radiation with that from the NoahMP-ref forcing further reduces the ground absorption of solar radiation (Figure 6d). These two factors together remove the enhanced melting during late-February to late-March (Figure 6b) and hence the strong snow ablation bias (Figure 6a) in the model, which confirms the mechanisms.

We also apply the aforementioned analyses to other sites with the same type of ablation bias (i.e., similar unobserved early-spring ablation in both WRF4km and NoahMP-WRFforc but not in NoahMP-ref). These analyses all have consistent results and conclusions with those at the Donkey Reservoir site shown above in terms of the causes of the ablation bias in WRF4km (Figures S11–S16 in Supporting Information S1). We note that even among the sites where precipitation underestimates exist in WRF4km, using wind speed and downward solar radiation from the NoahMP-ref forcing is effective to mitigate the early-spring melting events, while the remaining SWE underestimate is explained by the precipitation bias.

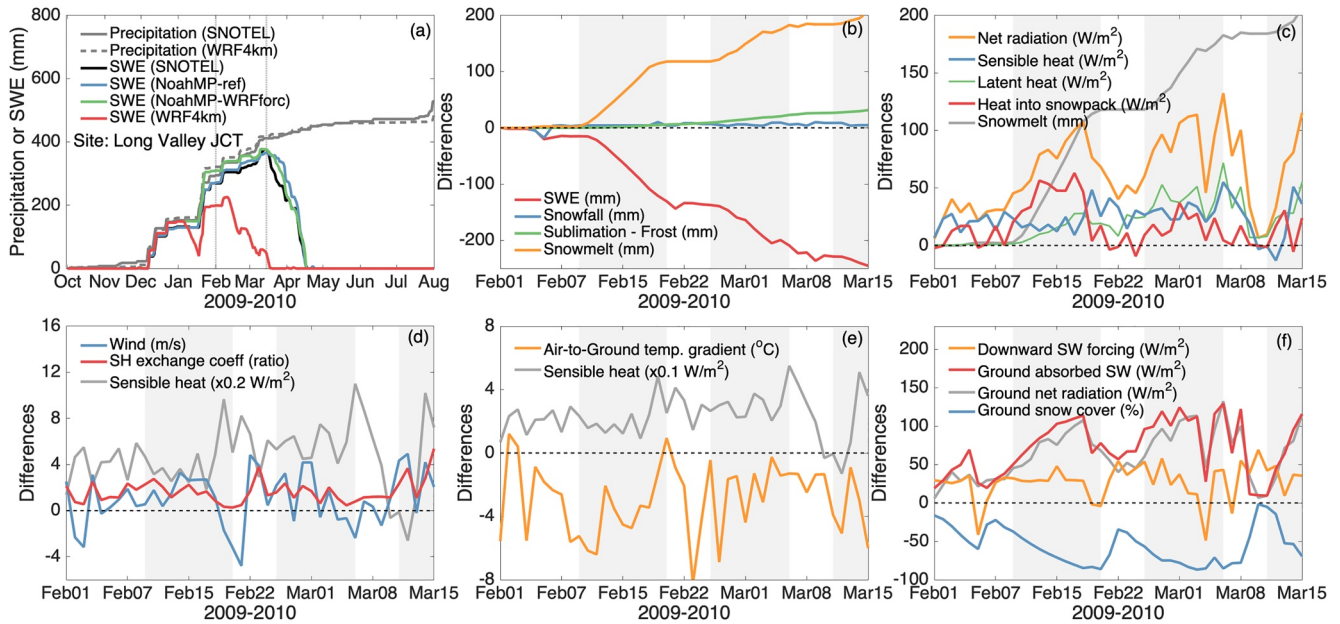


Figure 7. Same as Figure 5, but for the Long Valley SNOTEL site.

3.3. Sites With Ablation Bias Driven by Model Snow Parameterizations

Figure 7 shows early-spring snow surface energy and water budget analyses for a typical site (Long Valley JCT), where both NoahMP-ref and NoahMP-WRFforc accurately capture the observed SWE accumulation during November to April but WRF4km, albeit with small ($\sim 5\%$) precipitation bias, shows strong ablation starting around mid-February and continuing until mid-March (Figure 7a). The similarly good performance of NoahMP-ref and NoahMP-WRFforc suggests that the WRF4km forcing is not the driver of the WRF4km ablation bias at the site, whereas the difference between NoahMP-WRFforc and WRF4km is very likely due to differences in Noah-MP snow-related parameterizations. Water budget analyses that compare NoahMP-ref and WRF4km show that the early-spring ablation in WRF4km is still due to multiple strong melting events, with accumulated snowmelt of up to 100 mm within about 1 week for each event (Figure 7b). The strong melting is caused by the substantially enhanced surface net radiation and hence heat flux into snowpack (Figure 7c). This is different from the results in Section 3.2, where both enhanced net radiation and downward sensible heat flux contribute to the ablation bias. The enhanced net radiation in WRF4km at this site (Long Valley JCT) is dominantly driven by the lower surface albedo induced by stronger melting-induced snow cover reductions and thus higher ground absorption of solar radiation (Figure 7f). The significantly lower (by up to 80%) snow cover in WRF4km than NoahMP-ref is attributable to their differences in the Noah-MP snow parameterizations (Section 2.4.1). Specifically, the updated snow cover parameters, the improved surface roughness length, and the reduced snow compaction rate in NoahMP-ref all favor a higher snow cover compared with the earlier version of the Noah-MP snow parameterizations in WRF4km. The lower snow cover in WRF4km leads to a lower surface albedo and triggers a positive albedo feedback, highlighting the importance of snow cover and albedo feedback in SWE simulations. We note that the WRF4km downward solar radiation is slightly larger ($\sim 25 \text{ W m}^{-2}$) than NoahMP-ref, which, however, is not the main driver for the ablation bias because NoahMP-WRFforc using the WRF4km forcing does not show the ablation bias (Figure 7a).

Applying the preceding analyses to other sites with the same type of ablation bias (i.e., unobserved early-spring ablation in WRF4km but not in NoahMP-ref or NoahMP-WRFforc), we find consistent results and conclusions with those at the Long Valley JCT site shown above in terms of the causes of the WRF4km ablation bias (Figures S17 and S18 in Supporting Information S1). Even though the WRF4km precipitation is underestimated at some of those sites, simulations using the updated Noah-MP snow parameterizations (i.e., NoahMP-WRFforc) are still able to avoid the early-spring ablation bias (Figure S18a in Supporting

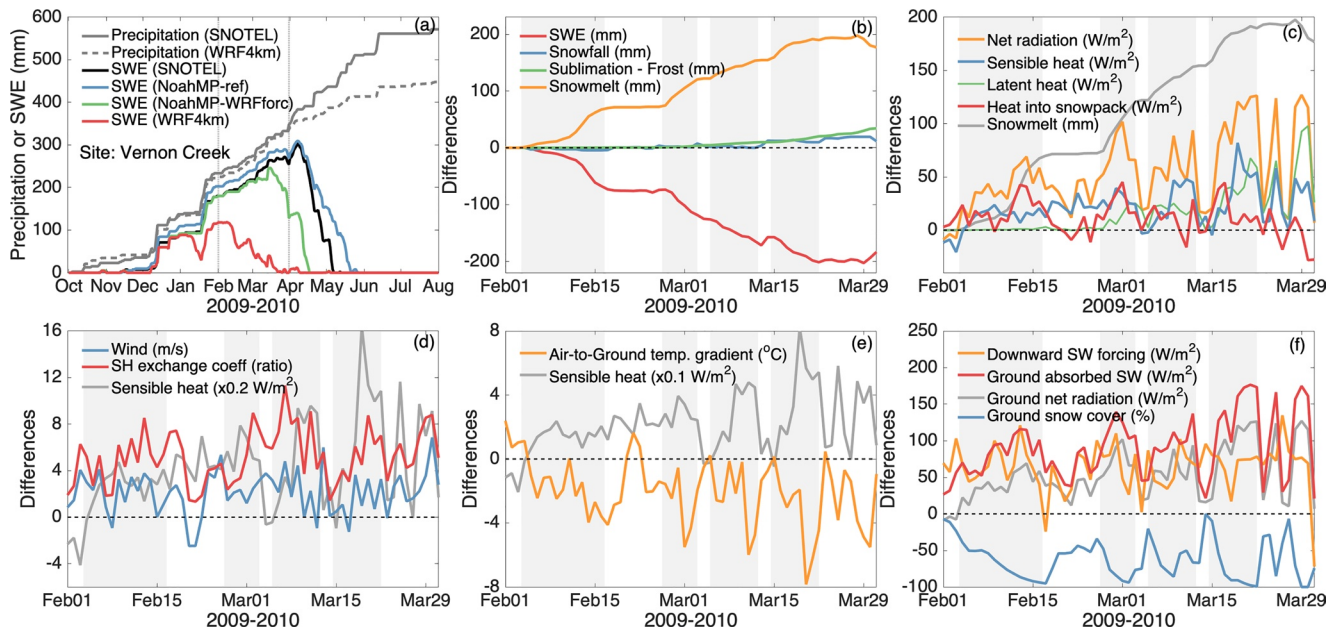


Figure 8. Same as Figure 5, but for the Vernon Creek SNOTEL site.

Information S1). This again suggests the dominant role of the model snow parameterizations in controlling the ablation behavior at these sites.

3.4. Sites With Ablation Bias Driven by Both Forcing and Snow Parameterizations

Using the similar energy and water budget analyses in Sections 3.2 and 3.3, we investigate the sites where NoahMP-ref reproduces the observed SWE accumulation, and WRF4km shows the ablation bias during mid-February to late-March, while NoahMP-WRFforc performs better than WRF4km with a smaller ablation bias. Figure 8 shows the analysis at a typical site (Vernon Creek) of this kind. The early-spring SWE improvement in NoahMP-WRFforc compared to WRF4km indicates the effect of Noah-MP snow parameterization updates in the reference model configuration on mitigating the ablation bias, while the remaining ablation bias in NoahMP-WRFforc compared to NoahMP-ref reveals the effect of the WRF4km forcing that favors the ablation bias (Figure 8a). We note that the observed precipitation is reproduced by WRF4km with <5% bias (Figure 8a). Similar to the results in Section 3.3, the WRF4km ablation at this site is due to a series of strong melting events in February and March (Figure 8b), which are driven by the significantly enhanced ground solar radiation absorption (Figure 8c). This enhanced ground absorption of solar radiation in WRF4km relative to NoahMP-ref is primarily due to both the higher downward solar radiation forcing (Figure 8f) and much less snow cover (by up to 100%) during melting (Figure 8f) that is caused by the differences in Noah-MP snow parameterizations as explained in Section 3.3.

On the other hand, NoahMP-WRFforc, albeit with a better SWE simulation than WRF4km due to the updates in Noah-MP snow parameterizations, still shows an ablation bias from mid-March to early April (Figure 9a). Analyses by comparing NoahMP-WRFforc and NoahMP-ref indicate that the ablation is driven by strong melting events (Figure 9b) contributed from the enhanced surface net radiation and downward sensible heat flux to snowpack surface (Figure 9c). The enhanced downward sensible heat flux mainly results from the higher (by up to a factor of 3) surface heat exchange coefficient induced by stronger (by up to 6 m s⁻¹) winds in the WRF4km forcing (Figure 9d). The enhanced surface net radiation is caused by the stronger ground absorption of solar radiation driven by the higher (by up to 120 W m⁻²) downward solar radiation in the WRF4km forcing (Figure 9f). Further sensitivity analyses confirm that replacing the WRF4km wind and downward solar radiation forcing with those from the NoahMP-ref forcing removes the early-spring ablation bias in NoahMP-WRFforc (Figure S19a in Supporting Information S1), mainly through reducing the ground solar radiation absorption (Figure S19d in Supporting Information S1) and the downward sensible

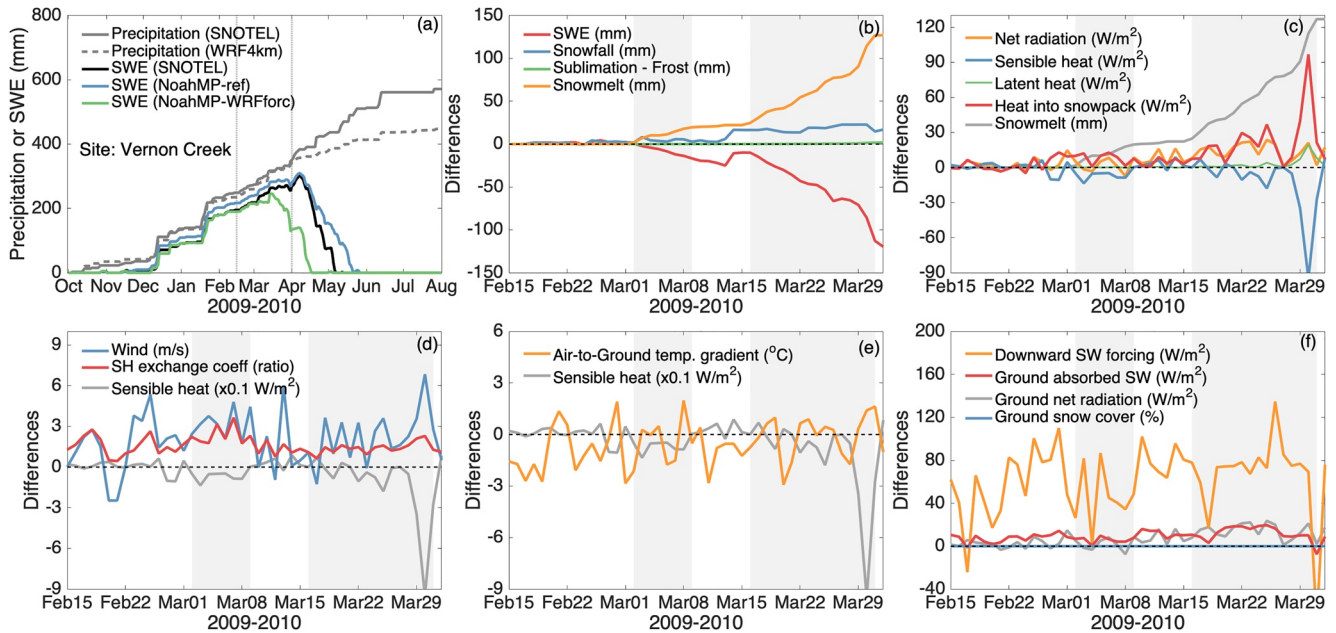


Figure 9. Same as Figure 8, but for analyses of the differences between NoahMP-WRFforc and NoahMP-ref.

heat flux to snowpack surface (Figure S19c in Supporting Information S1). Here, the mechanisms of the WRF4km forcing causing the ablation bias are consistent with those explained in Section 3.2.

Therefore, the early-spring WRF4km ablation bias is driven by biases in both Noah-MP snow parameterizations and atmospheric forcing (wind and downward solar radiation) at this site (Vernon Creek). We also apply the preceding analyses to other sites with the same bias type (i.e., unobserved early-spring ablation in WRF4km and NoahMP-WRFforc but not in NoahMP-ref, with NoahMP-WRFforc performing better than WRF4km). The results and conclusions (Figures S20–S23 in Supporting Information S1) regarding the causes of the early-spring WRF4km ablation bias are consistent with those at the Vernon Creek site presented above, even at sites with nontrivial precipitation underestimates in WRF4km.

3.5. Sites With Ablation Bias in the Reference Simulation

We notice that the unobserved early-spring ablation also exists in NoahMP-ref at some SNOTEL sites, which may reflect possible remaining deficiencies in the NoahMP-ref model physics and/or forcing. Thus, for those sites, we conduct similar energy and water budget analyses as done in Sections 3.2–3.4 to explore the causes. Figure 10 shows the analysis at a typical site (Rock Creek), where SWE starts to drop substantially in late February in NoahMP-ref which is not seen in observations (Figure 10a). This is driven by several strong melting events in NoahMP-ref during late February to late March (Figure 10b), which mainly results from the high downward sensible heat flux to snow surface to provide heat into snowpack that drives the melting (Figure 10c). The peaks of the downward sensible heat flux correspond well with the peaks of wind speed and below-canopy heat exchange coefficient (Figure 10d), suggesting a similar mechanism causing the WRF4km ablation (Section 3.2) where strong winds lead to enhanced sensible heat exchange coefficient and hence sensible heat flux. The positive air-to-ground temperature gradient determines the downward direction of the sensible heat flux (Figure 10e). We find that the ground net radiation is mostly negative in late February to late March (Figure 10c), indicating the ground losing net radiative energy during most of this period and hence a rather small contribution of surface radiation to the enhanced melting at this site. Further sensitivity analyses show that limiting the wind forcing to $\leq 2 \text{ m s}^{-1}$ substantially reduces the below-canopy heat exchange coefficient and hence downward sensible heat flux to snow surface (Figures 11c), leading to a much weaker melting (Figures 11b) and thus the removal of the ablation bias during late February to late March (Figures 11a). The air-to-ground temperature gradient does not show big changes in the sensitivity test. However, this sensitivity analysis does not necessarily mean that the NoahMP-ref wind

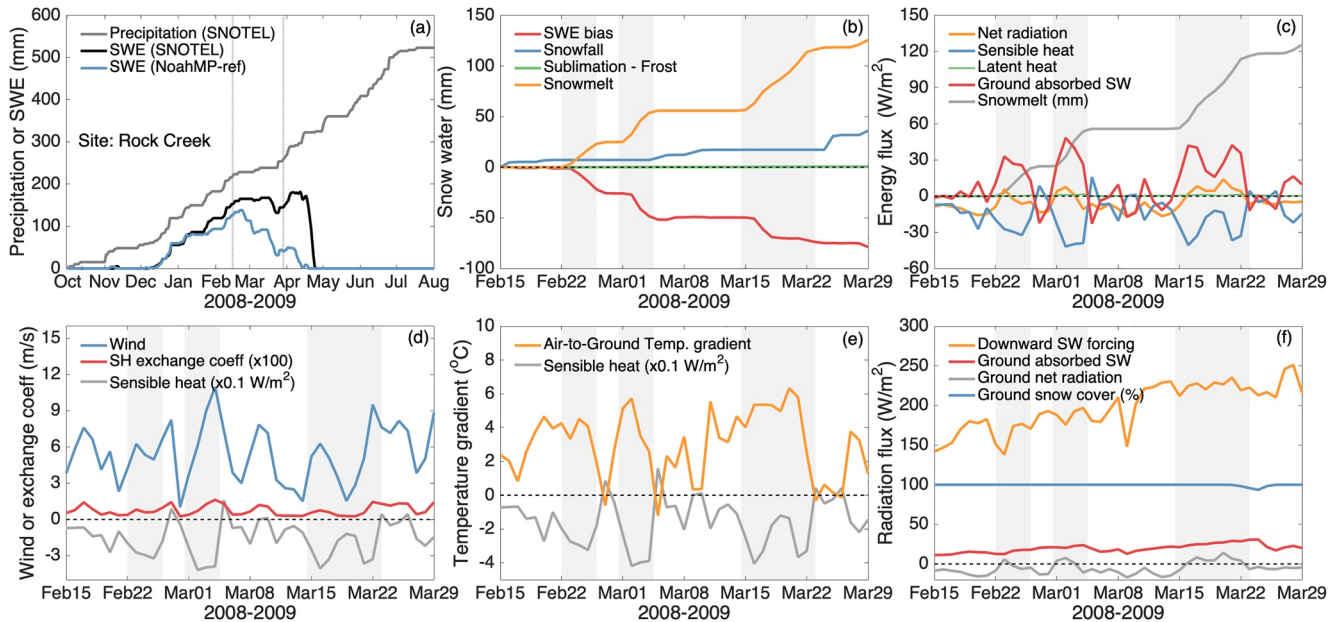


Figure 10. Energy and water budget analyses for Noah-MP reference simulations (NoahMP-ref) at the Rock Creek SNOTEL site. (a) Daily precipitation from observations (gray) and SWE from observations (black) and NoahMP-ref (blue). (b) SWE bias (red; NoahMP-ref minus observation) and NoahMP-ref simulated snowfall (blue), net sublimation (green), and snowmelt (orange) accumulated since February 15. Shaded time periods in (b)–(f) indicate melting events in NoahMP-ref. (c) NoahMP-ref simulated daily mean net radiation (orange), sensible heat (blue), latent heat (green), and heat into snowpack (red) at snowpack surface. The melting curve (gray line) is shown as a reference. (d) NoahMP-ref simulated daily mean wind speed (blue) and below-canopy sensible heat (SH) exchange coefficient (red). The sensible heat curve (gray line) is shown as a reference. (e) Same as panel (d), but for temperature gradient from air to ground (orange). (f) NoahMP-ref simulated daily mean ground absorbed shortwave (SW) radiation (red), net total radiation (gray), snow cover fraction (blue), and downward SW radiation forcing (orange).

forcing is biased high, since limiting the wind speed to $\leq 2 \text{ m s}^{-1}$ may not be realistic and the representation of other relevant processes such as the below-canopy turbulence may also have errors (see Section 4 for more discussions). This at least highlights the important role of wind forcing and/or wind-relevant processes in driving the early-spring ablation bias in NoahMP-ref. The preceding mechanisms and conclusions are also true for other sites with the similar bias patterns (Figures S24–S29 in Supporting Information S1).

Besides, we find that in addition to the downward sensible heat, the strong ground absorption of solar radiation at some sites can also have important contributions to the enhanced snow melting in NoahMP-ref (Figure 12 and Figures S30–S35 in Supporting Information S1). Sensitivity analyses indicate that reducing wind speed at these sites only partially reduces the early-spring ablation bias in NoahMP-ref, whereas further reducing the downward solar radiation forcing by 20% can remove the ablation bias during late February to late March due to the decrease of ground solar radiation absorption (Figure 13 and Figures S30–S35 in Supporting Information S1). Again, this sensitivity analysis does not necessarily mean that the NoahMP-ref downward solar radiation forcing is biased high, because other relevant processes such as the canopy radiative transfer and/or snow albedo parameterizations may also have errors (see Section 4 for more discussions).

4. Uncertainty and Implication for Model Improvement

Our analyses of the WRF4km ablation bias in this study rely on the comparison with the reference simulation (NoahMP-ref) that reproduces the observed SWE evolution. This raises a few cautions. First, NoahMP-ref accurately captures the observed SWE at most sites, but it might be due to the offset of model biases in different processes. We note that systematical Noah-MP model assessments and intercomparison with other LSMs from previous studies (e.g., Chen et al., 2014; Xiao et al., 2021) demonstrate a relatively good performance of Noah-MP in snow simulations, providing confidence in the accuracy of most Noah-MP model processes. However, further model improvements in snow-relevant processes are still needed, such

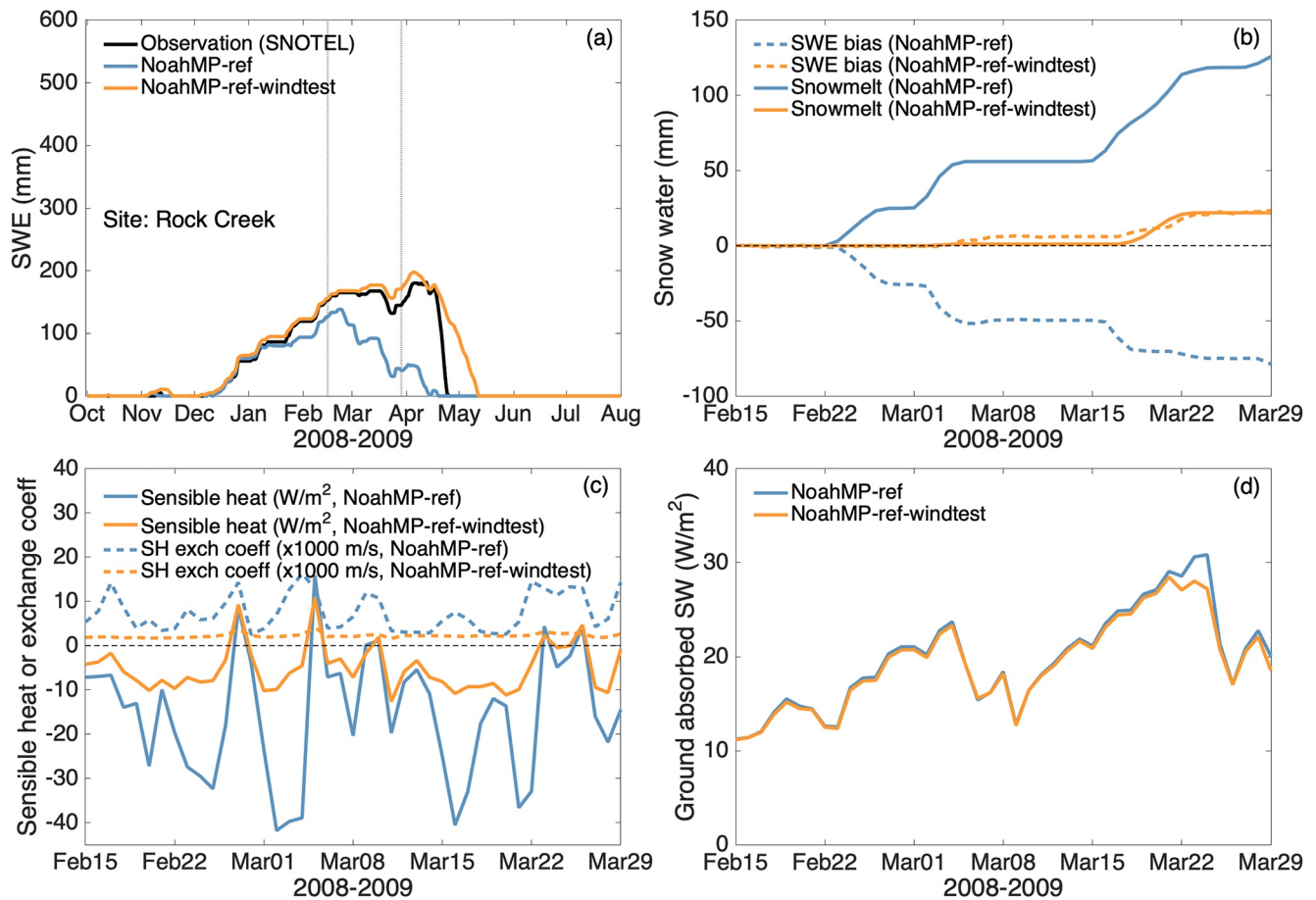


Figure 11. Sensitivity analyses at the Rock Creek SNOTEL site for Noah-MP reference simulations (blue; NoahMP-ref) and Noah-MP simulations driven by the reference forcing but with wind speed forcing limited to $\leq 2 \text{ m s}^{-1}$ (orange; NoahMP-ref-windtest). (a) Daily precipitation from observations (gray) and SWE from observations (black), NoahMP-ref, and NoahMP-ref-windtest. (b) SWE bias (dashed lines; model minus observation) and simulated snowmelt (solid lines) accumulated since February 15 from NoahMP-ref and NoahMP-ref-windtest. (c) Same as panel (b), but for daily mean below-canopy sensible heat (solid lines) and exchange coefficient (dashed lines; scaled by 1,000). (d) Same as panel (b), but for daily mean ground absorbed shortwave (SW) radiation.

as parameterizations of snow albedo and canopy-snow processes (see below for more discussions). Second, the optimization of NoahMP-ref heavily relies on the NLDAS-2 data downscaled from the NLDAS-2 data to 90-m resolution with both topographic adjustments and the scaling of precipitation and temperature to match observations, but these forcing conditions may still have errors. We note that substantial efforts have been made to improve the NLDAS-2 forcing through assimilating ground and satellite observations, which shows a reasonably good performance and hence has been widely used (Xia et al., 2012). The forcing downscaling procedure by accounting for topography also follows the widely used methodology proposed by Liston and Elder (2006) and Gupta and Tarboton (2016), which demonstrates sufficient accuracy. Nevertheless, without comprehensive in-situ measurements of the forcing variables (particularly wind and solar radiation), it is difficult to conduct systematic evaluation of the NoahMP-ref and WRF4km forcing. This further calls for more meteorological observation networks (e.g., for wind and solar radiation) over the western U.S. mountain ranges to facilitate future snow analysis in these regions. Even though some SNOTEL sites are enhanced with wind speed and/or solar radiation measurements, those data are not available for the Utah sites during the time period analyzed in this study. Some previous studies (e.g., He, Chen, et al., 2019; Lundquist et al., 2019) also demonstrated the value of using the gridded convection-permitting modeling products as forcing for simulating snowpack in western U.S. complex-terrain mountain ranges.

Despite those uncertainties, the comparison between WRF4km and NoahMP-ref still sheds light on the important roles of wind and downward solar radiation forcing as well as snow cover reduction in causing the early-spring ablation bias in WRF4km (Sections 3.2–3.4). Moreover, the suite of sensitivity analyses by

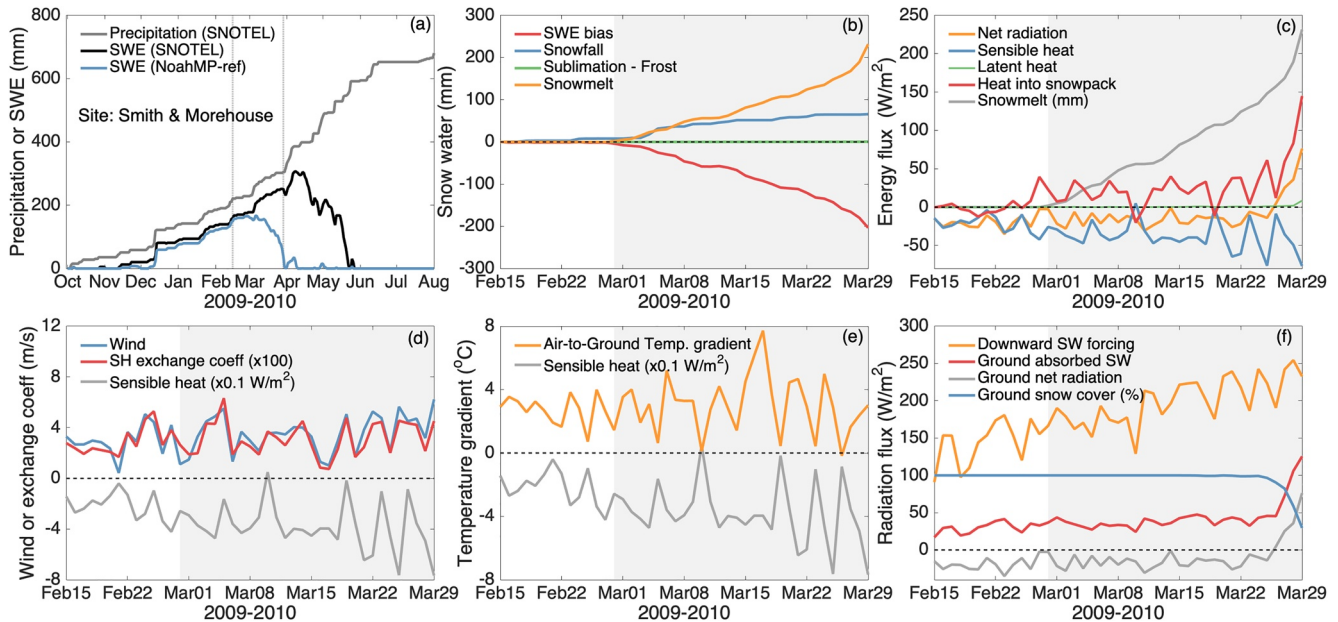


Figure 12. Same as Figure 10, but for the Smith and Morehouse SNOTEL site. Shaded time periods in (b)–(f) indicate melting events in NoahMP-ref.

varying wind and solar radiation forcing and model snow parameterizations further confirm the proposed mechanisms (Sections 3.2–3.4), which provides additional assurance of the quality of our conclusions. The surface wind bias in WRF4km suggests potential model deficiencies in surface and planetary boundary layer parameterizations, while the bias in downward surface solar radiation points toward potential model weakness in cloud microphysics and/or canopy processes. This provides implications for future improvements of WRF model physics and configurations. We should caution that although our results reveal the dominant role of wind and solar radiation in driving the strong melting, it does not imply that precipitation and temperature are not important. Instead, precipitation and temperature are two major drivers of SWE evolution. However, in this study, the early-spring WRF4km ablation bias occurs even without noticeable model biases in precipitation and surface temperature.

On the other hand, the analysis of the ablation bias in NoahMP-ref (Section 3.5) suggests that reducing wind and downward solar radiation in the reference forcing can remove the bias via decreasing downward sensible heat flux and ground solar radiation absorption. However, this does not necessarily mean that the wind and solar radiation forcing are overestimated in the reference forcing. For example, limiting the wind forcing to $\leq 2 \text{ m s}^{-1}$ in the sensitivity analysis is a very strong constraint that may not be realistic. Thus, in addition to the possible bias in atmospheric forcing, the NoahMP-ref bias analysis also implies possible deficiencies in Noah-MP physics. For instance, the canopy-wind interaction and below-canopy turbulence calculations may be biased, while a stronger aerodynamic resistance to sensible heat throughout the canopy could achieve a similar effect of reducing wind forcing on mitigating the ablation bias. In a companion work (Abolafia-Rosenzweig et al., 2021), we are improving the Noah-MP canopy turbulence scheme and test its impact on snowpack simulations. Besides, the canopy radiative transfer process along with canopy properties (e.g., leaf area index, canopy height and vegetation cover) may also be biased in the model, while a stronger blocking of downward solar radiation during the canopy radiative transfer could achieve a similar effect of decreasing solar radiation forcing on reducing the ablation bias. Previous studies (e.g., Chen et al., 2014; Essery et al., 2009) have suggested that canopy processes (e.g., below-canopy turbulence, radiative transfer, and interception) are among the most important uncertainty sources affecting snowpack simulations in LSMs. Furthermore, snow albedo bias in Noah-MP may also contribute to the bias in ground solar radiation absorption that drives the early-spring ablation bias. Several studies have highlighted the important role of snow albedo in the uncertainty of Noah-MP snowpack simulations (e.g., Chen et al., 2014; He, Chen, et al., 2019; Jiang et al., 2020). One particular complication in snow albedo modeling is dust deposition on snowpack in the western U.S., which significantly reduces snow albedo during dust events

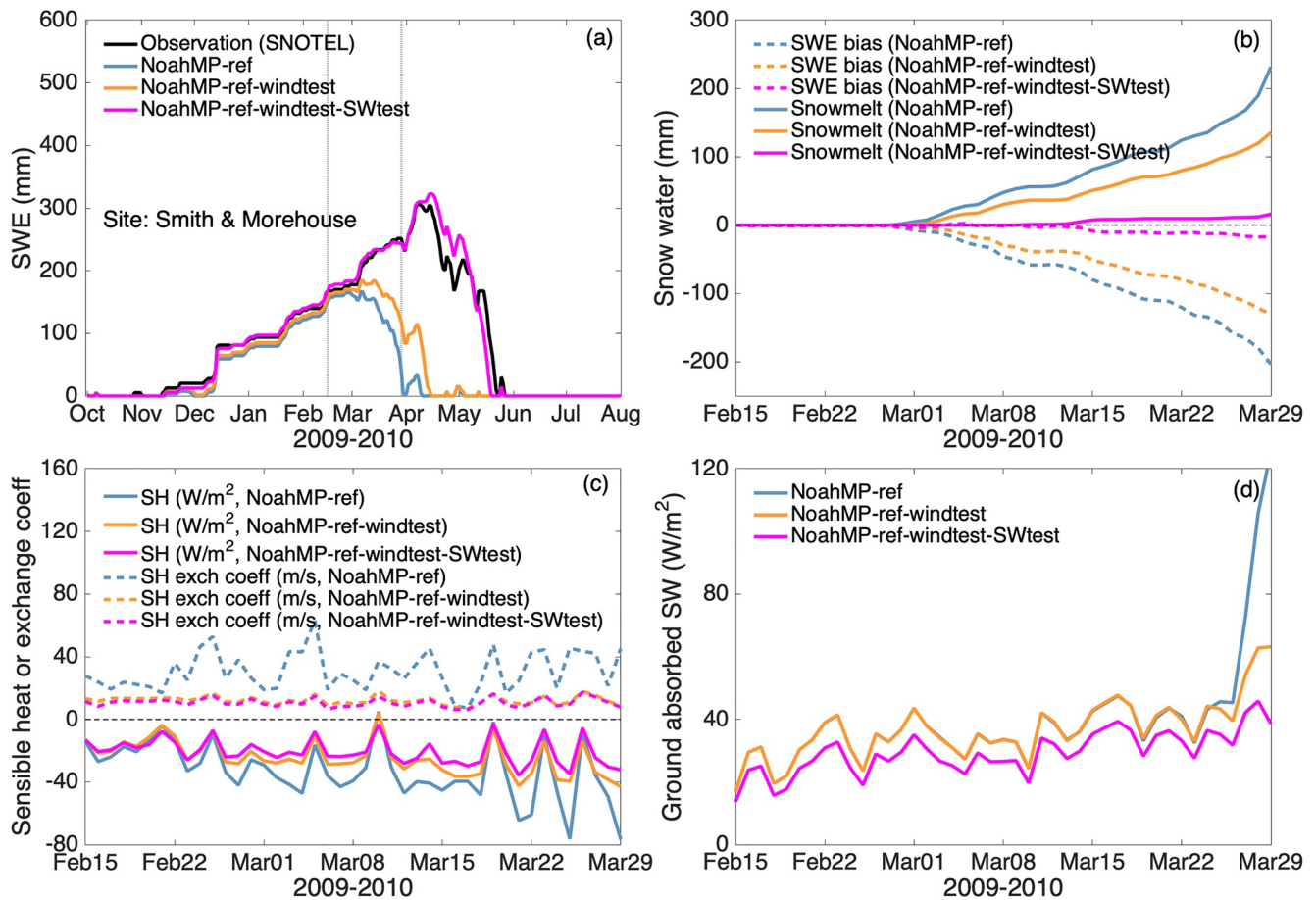


Figure 13. Same as Figure 11, but for the Smith and Morehouse SNOTEL site. Also shown are the results from Noah-MP simulations driven by the reference forcing but with wind speed forcing limited to $\leq 2 \text{ m s}^{-1}$ and downward solar radiation forcing reduced by 20% (magenta; NoahMP-ref-windtest-SWtest). The sensible heat (SH) exchange coefficient in panel (c) is scaled up by 1000.

(Liou et al., 2014; Painter et al., 2018). This process, however, is not explicitly represented in Noah-MP and will be investigated in our future study. In an on-going work, we are improving the snow albedo scheme in Noah-MP using in-situ surface spectral radiation measurements over a Colorado mountain.

Overall, the analysis in this study reveals that deficiencies in atmospheric forcing and/or model snow physics lead to an excess of energy being input to the simulated snowpack, initiating the unobserved early-spring snow melting. Such melting further reduces the snow cover, substantially increases grid-scale surface absorption of solar radiation, and hence further accelerates the melting. This highlights the importance of snow albedo feedback in causing the rapid snow melting during early spring.

Snowpack simulations may be dominated by different model processes or parameters (Sun et al., 2019) over different climate regimes. As a result, the reference model configuration optimized by using the entire western U.S. SNOTEL measurements may not be optimal for Utah simulations (as partly reflected in Figure 4a) and may introduce uncertainty to our analysis. We conducted additional sensitivity tests by further tuning snow-related model parameters to minimize discrepancies relative to observations averaged over the Utah sites, which however do not show significant improvements compared to the reference simulation. This is probably due to potential intrinsic deficiencies in model physics and representations of snow albedo and canopy/vegetation characteristics and processes (e.g., canopy radiative transfer, turbulence, and interception) as discussed above. Comprehensive diagnosis and improvement of these Noah-MP processes are outside the scope of this study and require future investigation.

Moreover, our assessment of the site features (e.g., vegetation type and topography) does not reveal any distinct vegetation or topographic patterns related to the ablation bias. It will be useful, in future work, to extend the analysis conducted here to the entire western U.S. mountain ranges, which provides an opportunity to more comprehensively investigate the site characteristics related to the WRF4km early-spring snow ablation bias. Although we use the very high-resolution (30-m) NLCD vegetation type and USGS DEM topography datasets in the simulations, attempting to capture the real site condition, model errors in representing canopy properties (e.g., canopy height and leaf area index) and related processes (e.g., canopy radiative transfer, turbulence, and snow interception) may still contribute to the ablation bias. Indeed, as discussed above, changes to atmospheric forcing (i.e., solar radiation and wind speeds) in NoahMP-ref may improve model performance by compensating for errors caused by vegetation/canopy misrepresentation or deficient parameterizations.

5. Conclusions

In this study, we conducted process-level snowpack analyses of the convection-permitting (4-km) NCAR WRF CONUS simulations (WRF4km) at Utah SNOTEL sites to understand the mechanisms causing the unobserved strong early-spring snow ablation in WRF4km. To assist in the snow ablation analysis, we also conducted a suite of Noah-MP simulations for intercomparison with WRF4km. The analysis further showed important implications for future model improvements. Overall, our main conclusions are as follows:

1. The unobserved strong snow ablation during early spring (mid-February to late-March) in WRF4km over Utah mountains is driven by multiple strong melting events. The melting events are mainly caused by both the enhanced downward sensible heat flux to snowpack surface and the enhanced ground absorption of solar radiation in WRF4km. Their relative contributions vary across different sites and time periods. In general, the contribution of the enhanced downward sensible heat flux tends to be more significant before early March, while the contribution of the enhanced ground solar radiation absorption increases from February to March and tends to be dominant after early March.
2. The enhanced downward sensible heat flux to snow surface primarily results from the enhanced below-canopy heat exchange coefficient induced by strong surface winds in WRF4km. The enhanced ground absorption of solar radiation in WRF4km is due to both strong downward surface solar radiation and strong melting-induced snow cover reduction caused by the earlier version of Noah-MP snow-related parameterizations and parameters used in WRF4km. The increasing importance of the enhanced ground solar radiation absorption from February to April and the associated temporal variation are dominated by the substantial snow cover reduction during melting, which decreases surface albedo and triggers a positive albedo feedback that further accelerates melting.
3. The early-spring ablation bias in the reference Noah-MP simulation is also caused by strong melting events that result from strong downward sensible heat flux to snow surface and/or ground absorption of solar radiation. This suggests possible biases in the wind and solar radiation forcing, and/or potential deficiencies in Noah-MP snow-related physics, including representations of below-canopy turbulence, canopy radiative transfer, snow interception by canopy, and snow albedo. The analysis and methodology in this study can be applied to diagnosing model snow ablation biases over other regions, and shed light on possible directions for future WRF and Noah-MP model improvements.

Conflict of Interest

The authors declare no conflicts of interest relevant to this study.

Data Availability Statement

The authors thank Z. Zhang for helping with 4-km WRF CONUS data transfer, which are available at <https://rda.ucar.edu/datasets/ds612.0/>. The bias-corrected and quality-controlled SNOTEL data is available at <https://www.pnnl.gov/data-products>. The model data produced by this study is available via the public repository (<https://osf.io/bqenw/>). The authors would like to acknowledge high performance computing

support from Cheyenne (doi:10.5065/D6RX99HX) provided by NCAR's Computational and Information Systems Laboratory, sponsored by the National Science Foundation.

Acknowledgments

This research was funded by the NCAR Water System and the NOAA Grants NA18OAR4590381, NA18OAR4310134 and NA20OAR4310421. NCAR is sponsored by the National Science Foundation. Any opinions, findings, conclusions, or recommendations expressed in this publication are those of the authors and do not necessarily reflect the views of the National Science Foundation.

References

Abolafia-Rosenzweig, R., He, C., Burns, S., & Chen, F. (2021). Implementation and evaluation of a unified turbulence parameterization throughout the canopy and roughness sublayer in Noah-MP snow simulations. *Journal of Advances in Modeling Earth Systems*. <https://doi.org/10.1029/2021ms002665>

Anderson, E. A. (1976). *A point energy and mass balance model of a snow cover* NOAA Technical Report NWS 19, Office of Hydrology. National Weather Service. <https://repository.library.noaa.gov/view/noaa/6392>

Bales, R. C., Molotch, N. P., Painter, T. H., Dettinger, M. D., Rice, R., & Dozier, J. (2006). Mountain hydrology of the western United States. *Water Resources Research*, 42(8), 1–13. <https://doi.org/10.1029/2005WR004387>

Barnett, T. P., Adam, J. C., & Lettenmaier, D. P. (2005). Potential impacts of a warming climate on water availability in snow-dominated regions. *Nature*, 438, 303–309. <https://doi.org/10.1038/nature04141>

Barnhart, T. B., Molotch, N. P., Livneh, B., Harpold, A. A., Knowles, J. F., & Schneider, D. (2016). Snowmelt rate dictates streamflow. *Geophysical Research Letters*, 43(15), 8006–8016. <https://doi.org/10.1002/2016gl069690>

Burles, K., & Boon, S. (2011). Snowmelt energy balance in a burned forest plot, Crowsnest Pass, Alberta, Canada. *Hydrological Processes*, 25(19), 3012–3029. <https://doi.org/10.1002/hyp.8067>

Chen, F., Barlage, M., Tewari, M., Rasmussen, R., Jin, J., Lettenmaier, D., et al. (2014). Modeling seasonal snowpack evolution in the complex terrain and forested Colorado Headwaters region: A model intercomparison study. *Journal of Geophysical Research - D: Atmospheres*, 119, 13795–13819. <https://doi.org/10.1002/2014JD022167>

Chen, F., & Dudhia, J. (2001). Coupling an advanced land surface–hydrology model with the Penn State-NCAR MM5 modeling system. Part I: Model implementation and sensitivity. *Monthly Weather Review*, 129(4), 569–585. [https://doi.org/10.1175/1520-0493\(2001\)129<0569:caalsh>2.0.co;2](https://doi.org/10.1175/1520-0493(2001)129<0569:caalsh>2.0.co;2)

Chen, F., Janjić, Z., & Mitchell, K. (1997). Impact of atmospheric surface-layer parameterizations in the new land-surface scheme of the NCEP mesoscale Eta model. *Boundary-Layer Meteorology*, 85(3), 391–421. <https://doi.org/10.1023/a:1000531001463>

Chen, F., Mitchell, K., Schaake, J., Xue, Y., Pan, H.-L., Koren, V., et al. (1996). Modeling of land surface evaporation by four schemes and comparison with FIFE observations. *Journal of Geophysical Research: Atmospheres*, 101, 7251–7268. <https://doi.org/10.1029/95JD02165>

Chen, F., & Zhang, Y. (2009). On the coupling strength between the land surface and the atmosphere: From viewpoint of surface exchange coefficients. *Geophysical Research Letters*, 36, L10404. <https://doi.org/10.1029/2009GL037980>

Chen, X., Leung, L. R., Wigmosta, M., & Richmond, M. (2019). Impact of atmospheric rivers on surface hydrological processes in western US watersheds. *Journal of Geophysical Research: Atmospheres*, 124(16), 8896–8916. <https://doi.org/10.1029/2019jd030468>

Clark, M. P., Hendrikx, J., Slater, A. G., Kavetski, D., Anderson, B., Cullen, N. J., et al. (2011). Representing spatial variability of snow water equivalent in hydrologic and land-surface models: A review. *Water Resources Research*, 47, W07539. <https://doi.org/10.1029/2011WR010745>

Dee, D. P., Uppala, S. M., Simmons, Berrisford, P., Poli, P., Kobayashi, S., et al. (2011). The ERA-Interim reanalysis: Configuration and performance of the data assimilation system. *Quarterly Journal of the Royal Meteorological Society*, 137(656), 553–597. <https://doi.org/10.1002/qj.828>

Dickinson, R. E., Henderson-Sellers, A., & Kennedy, P. J. (1993). *Biosphere-Atmosphere Transfer Scheme (BATS) version 1e as coupled to the NCAR Community Climate Model*, NCAR Tech. Note NCAR/TN- 387+STR (p. 80). National Center for Atmospheric Research. <https://doi.org/10.5065/D67W6959>

Eidhammer, T., Grubišić, V., Rasmussen, R., & Ikeda, K. (2018). Winter precipitation efficiency of mountain ranges in the Colorado Rockies under climate change. *Journal of Geophysical Research: Atmospheres*, 123, 2573–2590. <https://doi.org/10.1002/2017JD027995>

Ek, M. B., Mitchell, K. E., Lin, Y., Rogers, E., Grunmann, P., Koren, V., et al. (2003). Implementation of Noah land surface model advances in the National Centers for Environmental Prediction operational mesoscale Eta model. *Journal of Geophysical Research*, 108(D22). <https://doi.org/10.1029/2002jd003296>

Essery, R., Rutter, N., Pomeroy, J., Baxter, R., Stähli, M., Gustafsson, D., et al. (2009). SNOWMIP2: An evaluation of forest snow process simulations. *Bulletin of the American Meteorological Society*, 90(8), 1120–1136. <https://doi.org/10.1175/2009bams2629.1>

Gergel, D. R., Nijssen, B., Abatzoglou, J. T., Lettenmaier, D. P., & Stumbaugh, M. R. (2017). Effects of climate change on snowpack and fire potential in the western USA. *Climatic Change*, 141(2), 287–299. <https://doi.org/10.1007/s10584-017-1899-y>

Gupta, A. S., & Tarboton, D. G. (2016). A tool for downscaling weather data from large-grid reanalysis products to finer spatial scales for distributed hydrological applications. *Environmental Modelling & Software*, 84, 50–69. <https://doi.org/10.1016/j.envsoft.2016.06.014>

Harpold, A. A., Biederman, J. A., Condon, K., Merino, M., Korgaonkar, Y., Nan, T., et al. (2014). Changes in snow accumulation and ablation following the Las Conchas Forest Fire, New Mexico, USA. *Ecohydrology*, 7(2), 440–452. <https://doi.org/10.1002/eco.1363>

He, C., Chen, F., Barlage, M., Liu, C., Newman, A., Tang, W., et al. (2019). Can convection-permitting modeling provide decent precipitation for offline high-resolution snowpack simulations over mountains? *Journal of Geophysical Research: Atmospheres*, 124(23), 12631–54. <https://doi.org/10.1029/2019JD030823>

He, C., Liou, K. N., Takano, Y., Chen, F., & Barlage, M. (2019). Enhanced snow absorption and albedo reduction by dust-snow internal mixing: Modeling and parameterization. *Journal of Advances in Modeling Earth Systems*, 11(11), 3755–3776. <https://doi.org/10.1029/2019ms001737>

He, C., Liou, K. N., Takano, Y., Yang, P., Qi, L., & Chen, F. (2018). Impact of grain shape and multiple black carbon internal mixing on snow albedo: Parameterization and radiative effect analysis. *Journal of Geophysical Research: Atmospheres*, 123, 1253–1268. <https://doi.org/10.1002/2017JD027752>

Hong, S. Y., Noh, Y., & Dudhia, J. (2006). A new vertical diffusion package with an explicit treatment of entrainment processes. *Monthly Weather Review*, 134(9), 2318–2341. <https://doi.org/10.1175/mwr3199.1>

Iacono, M. J., Delamere, J. S., Mlawer, E. J., Shephard, M. W., Clough, S. A., & Collins, W. D. (2008). Radiative forcing by long-lived greenhouse gases: Calculations with the AER radiative transfer models. *Journal of Geophysical Research*, 113, D13103. <https://doi.org/10.1029/2008JD009944>

Ikeda, K., et al. (2021). Snowfall and snowpack in the Western US as captured by convection permitting climate simulations: Current climate and pseudo global warming future climate. *Climate Dynamics*, 1–25. <https://doi.org/10.1007/s00382-021-05805-w>

- Ikeda, K., Rasmussen, R., Liu, C., Gochis, D., Yates, D., Chen, F., et al. (2010). Simulation of seasonal snowfall over Colorado. *Atmospheric Research*, 97(4), 462–477. <https://doi.org/10.1016/j.atmosres.2010.04.010>
- Jiang, Y., Chen, F., Gao, Y., He, C., Barlage, M., & Huang, W. (2020). Assessment of uncertainty sources in snow cover simulation in the Tibetan Plateau. *Journal of Geophysical Research: Atmospheres*, 125(18), e2020JD032674. <https://doi.org/10.1029/2020jd032674>
- Jimenez, P. A., Dudhia, J. J., Gonzalez-Rouco, F., Navarro, J., Montavez, J. P., & Garcia-Bustamante, E. (2012). A revised scheme for the WRF surface layer formulation. *Monthly Weather Review*, 140, 898–918. <https://doi.org/10.1175/MWR-D-11-00056.1>
- Jing, X., Geerts, B., Wang, Y., & Liu, C. (2017). Evaluating seasonal orographic precipitation in the interior western United States using gauge data, gridded precipitation estimates, and a regional climate simulation. *Journal of Hydrometeorology*, 18, 2541–2558. <https://doi.org/10.1175/JHM-D-17-0056.1>
- Jordan, R. (1991). *A one-dimensional temperature model for a snow cover*, Spec. Rep. 91–16, Cold Reg. Res. and Eng. Lab. U.S. Army Corps of Engineers. <https://hdl.handle.net/11681/11677>
- Li, D., Wrzesien, M. L., Durand, M., Adam, J., & Lettenmaier, D. P. (2017). How much runoff originates as snow in the western United States, and how will that change in the future? *Geophysical Research Letters*, 44, 6163–6172. <https://doi.org/10.1002/2017gl073551>
- Liou, K. N., Takano, Y., He, C., Yang, P., Leung, L. R., Gu, Y., & Lee, W. L. (2014). Stochastic parameterization for light absorption by internally mixed BC/dust in snow grains for application to climate models. *Journal of Geophysical Research: Atmospheres*, 119(12), 7616–7632. <https://doi.org/10.1002/2014JD021665>
- Liston, G. E. (2004). Representing subgrid snow cover heterogeneities in regional and global models. *Journal of Climate*, 17(6), 1381–1397. [https://doi.org/10.1175/1520-0442\(2004\)017<1381:rsschi>2.0.co;2](https://doi.org/10.1175/1520-0442(2004)017<1381:rsschi>2.0.co;2)
- Liston, G. E., & Elder, K. (2006). A meteorological distribution system for high-resolution terrestrial modeling (MicroMet). *Journal of Hydrometeorology*, 7(2), 217–234. <https://doi.org/10.1175/jhm486.1>
- Liu, C., Ikeda, K., Rasmussen, R., Barlage, M., Newman, A. J., Prein, A. F., et al. (2017). Continental-scale convection-permitting modeling of the current and future climate of North America. *Climate Dynamics*, 49, 71–95. <https://doi.org/10.1007/s00382-016-3327-9>
- Liu, C., Ikeda, K., Thompson, G., Rasmussen, R., & Dudhia, J. (2011). High-resolution simulations of wintertime precipitation in the Colorado Headwaters region: Sensitivity to physics parameterizations. *Monthly Weather Review*, 139, 3533–3553. <https://doi.org/10.1175/MWR-D-11-00009.1>
- Livneh, B., & Badger, A. M. (2020). Drought less predictable under declining future snowpack. *Nature Climate Change*, 10(5), 452–458. <https://doi.org/10.1038/s41558-020-0754-8>
- Luce, C. H., & Holden, Z. A. (2009). Declining annual streamflow distributions in the Pacific Northwest United States, 1948–2006. *Geophysical Research Letters*, 36(16). <https://doi.org/10.1029/2009gl0139407>
- Lundquist, J., Hughes, M., Gutmann, E., & Kapnick, S. (2019). Our skill in modeling mountain rain and snow is bypassing the skill of our observational networks. *Bulletin of the American Meteorological Society*, 100, 2473–2490. <https://doi.org/10.1175/BAMS-D-19-0001.1>
- Mazzotti, G., Currier, W. R., Deems, J. S., Pflug, J. M., Lundquist, J. D., & Jonas, T. (2019). Revisiting snow cover variability and canopy structure within forest stands: Insights from airborne lidar data. *Water Resources Research*, 55(7), 6198–6216. <https://doi.org/10.1029/2019wr024898>
- Molotch, N. P., Blanken, P. D., Williams, M. W., Turnipseed, A. A., Monson, R. K., & Margulis, S. A. (2007). Estimating sublimation of intercepted and sub-canopy snow using eddy covariance systems. *Hydrological Processes: International Journal*, 21(12), 1567–1575. <https://doi.org/10.1002/hyp.6719>
- Mote, P. W., Li, S., Lettenmaier, D. P., Xiao, M., & Engel, R. (2018). Dramatic declines in snowpack in the western US. *Climate and Atmospheric Science*, 1(1), 2. <https://doi.org/10.1038/s41612-018-0012-1>
- Musselman, K. N., Addor, N., Vano, J. A., & Molotch, N. P. (2021). Winter melt trends portend widespread declines in snow water resources. *Nature Climate Change*, 1–7. <https://doi.org/10.1038/s41558-021-01014-9>
- Musselman, K. N., Clark, M. P., Liu, C., Ikeda, K., & Rasmussen, R. (2017). Slower snowmelt in a warmer world. *Nature Climate Change*, 7(3), 214–219. <https://doi.org/10.1038/nclimate3225>
- Musselman, K. N., Lehner, F., Ikeda, K., Clark, M. P., Prein, A., Liu, C., et al. (2018). Projected increases and regime shifts in rain-on-snow flood potential over western North America. *Nature Climate Change*, 8, 808–812. <https://doi.org/10.1038/s41558-018-0236-4>
- Niu, G.-Y., & Yang, Z.-L. (2004). The effects of canopy processes on snow surface energy and mass balances. *Journal of Geophysical Research*, 109, D23111. <https://doi.org/10.1029/2004JD004884>
- Niu, G.-Y., & Yang, Z.-L. (2007). An observation-based formulation of snow cover fraction and its evaluation over large North American river basins. *Journal of Geophysical Research*, 112, D21101. <https://doi.org/10.1029/2007JD008674>
- Niu, G. Y., Yang, Z.-L., Mitchell, K. E., Chen, F., Ek, M. B., Barlage, M., et al. (2011). The community Noah land surface model with multi-parameterization options (Noah-MP): 1. Model description and evaluation with local-scale measurements. *Journal of Geophysical Research*, 116, D12109. <https://doi.org/10.1029/2010JD015139>
- Painter, T. H., Skiles, S. M., Deems, J. S., Bryant, A. C., & Landry, C. C. (2012). Dust radiative forcing in snow of the Upper Colorado River Basin: 1. A 6 year record of energy balance, radiation, and dust concentrations. *Water Resources Research*, 48(7). <https://doi.org/10.1029/2012wr011985>
- Painter, T. H., Skiles, S. M. K., Deems, J. S., Brandt, W. T., & Dozier, J. (2018). Variation in rising limb of Colorado river snowmelt runoff hydrograph controlled by dust radiative forcing in snow. *Geophysical Research Letters*, 45(2), 797–808. <https://doi.org/10.1002/2017GL075826>
- Pederson, G. T., Gray, S. T., Woodhouse, C. A., Betancourt, J. L., Fagre, D. B., Littell, J. S., et al. (2011). The unusual nature of recent snowpack declines in the North American Cordillera. *Science*, 333(6040), 332–335. <https://doi.org/10.1126/science.1201570>
- Prein, A. F., Langhans, W., Fossier, G., Ferrone, A., Ban, N., Goergen, K., et al. (2015). A review on regional convection-permitting climate modeling: Demonstrations, prospects, and challenges. *Reviews of Geophysics*, 53(2), 323–361. <https://doi.org/10.1002/2014rg000475>
- Qu, X., & Hall, A. (2006). Assessing snow albedo feedback in simulated climate change. *Journal of Climate*, 19(11), 2617–2630. <https://doi.org/10.1175/jcli3750.1>
- Rasmussen, R., Ikeda, K., Liu, C., Gochis, D., Clark, M., Dai, A., et al. (2014). Climate change impacts on the water balance of the Colorado headwaters: High-resolution regional climate model simulations. *Journal of Hydrometeorology*, 15, 1091–1116. <https://doi.org/10.1175/JHM-D-13-0118.1>
- Rasmussen, R., Liu, C., Ikeda, K., Gochis, D., Yates, D., Chen, F., et al. (2011). High-resolution coupled climate runoff simulations of seasonal snowfall over Colorado: A process study of current and warmer climate. *Journal of Climate*, 24(12), 3015–3048. <https://doi.org/10.1175/2010JCLI3985.1>
- Rhoades, A. M., Ullrich, P. A., & Zarzycki, C. M. (2018). Projecting 21st century snowpack trends in western USA mountains using variable-resolution CESM. *Climate Dynamics*, 50(1), 261–288. <https://doi.org/10.1007/s00382-017-3606-0>

- Serreze, M. C., Clark, M. P., Armstrong, R. L., McGinnis, D. A., & Pulwarty, R. S. (1999). Characteristics of the western United States snowpack from snowpack telemetry (SNOTEL) data. *Water Resources Research*, 35, 2145–2160. <https://doi.org/10.1029/1999WR900090>
- Stewart, I. T., Cayan, D. R., & Dettinger, M. D. (2005). Changes toward earlier streamflow timing across western North America. *Journal of Climate*, 18(8), 1136–1155. <https://doi.org/10.1175/jcli3321.1>
- Sun, F., Berg, N., Hall, A., Schwartz, M., & Walton, D. (2019). Understanding end-of-century snowpack changes over California's Sierra Nevada. *Geophysical Research Letters*, 46, 933–943. <https://doi.org/10.1029/2018GL080362>
- Sun, N., Yan, H., Wigmosta, M., Skaggs, R., Leung, R., & Hou, Z. (2019). Regional snow parameters estimation for large-domain hydrological applications in the western United States. *Journal of Geophysical Research: Atmospheres*, 124(10), 5296–5313. <https://doi.org/10.1029/2018JD030140>
- Sun, S., Jin, J., & Xue, Y. (1999). A simple snow-atmosphere-soil transfer model. *Journal of Geophysical Research: Atmospheres*, 104(D16), 19587–19597. <https://doi.org/10.1029/1999jd900305>
- Thompson, G., & Eidhammer, T. (2014). A study of aerosol impacts on clouds and precipitation development in a large winter cyclone. *Journal of the Atmospheric Sciences*, 71(10), 3636–3658. <https://doi.org/10.1175/jas-d-13-0305.1>
- van Kampenhout, L., Lenaerts, J. T., Lipscomb, W. H., Sacks, W. J., Lawrence, D. M., Slater, A. G., & van den Broeke, M. R. (2017). Improving the representation of polar snow and firn in the Community Earth System Model. *Journal of Advances in Modeling Earth Systems*, 9(7), 2583–2600. <https://doi.org/10.1002/2017ms000988>
- Verseghy, D. L. (1991). CLASS-A Canadian land surface scheme for GCMs: I. Soil model. *International Journal of Climatology*, 11, 111–133. <https://doi.org/10.1002/joc.3370110202>
- Wang, Y., Geerts, B., & Liu, C. (2018). A 30-year convection-permitting regional climate simulation over the interior western United States. Part I: Validation. *International Journal of Climatology*, 38(9), 3684–3704. <https://doi.org/10.1002/joc.5527>
- Webster, C., Rutter, N., Zahner, F., & Jonas, T. (2016). Modeling subcanopy incoming longwave radiation to seasonal snow using air and tree trunk temperatures. *Journal of Geophysical Research - D: Atmospheres*, 121(3), 1220–1235. <https://doi.org/10.1002/2015jd024099>
- Xia, Y., Mitchell, K., Ek, M., Sheffield, J., Cosgrove, B., Wood, E., et al. (2012). Continental-scale water and energy flux analysis and validation for the North American Land Data Assimilation System project phase 2 (NLDAS-2): 1. Intercomparison and application of model products. *Journal of Geophysical Research: Atmospheres*, 117(D3). <https://doi.org/10.1029/2011jd016048>
- Xiao, M., Mahanama, S. P., Xue, Y., Chen, F., & Lettenmaier, D. P. (2021). Modeling Snow Ablation over the Mountains of the Western United States: Patterns and Controlling Factors. *Journal of Hydrometeorology*, 22(2), 297–311. <https://doi.org/10.1175/jhm-d-19-0198.1>
- Xu, L., & Dirmeyer, P. (2011). Snow-atmosphere coupling strength in a global atmospheric model. *Geophysical Research Letters*, 38, L13401. <https://doi.org/10.1029/2011GL048049>
- Yan, H., Sun, N., Wigmosta, M., Skaggs, R., Hou, Z., & Leung, R. (2018). Next-generation intensity-duration-frequency curves for hydrologic design in snow-dominated environments. *Water Resources Research*, 54(2), 1093–1108. <https://doi.org/10.1002/2017wr021290>
- Zilitinkevich, S. S. (1995). Non-local turbulent transport: Pollution dispersion aspects of coherent structure of convective flows. In H. Power, N. Moussiopoulos, & C. A. Brebbia (Eds.), *Air Pollution III Air pollution theory and simulations* (Vol. I, pp. 53–60). Computational Mechanics Publisher. <https://doi.org/10.2495/AIR950071>